

# Non-Abelian Ball-Chiu vertex for arbitrary Euclidean momenta

A. C. Aguilar,<sup>1</sup> J. C. Cardona,<sup>1</sup> M. N. Ferreira,<sup>1</sup> and J. Papavassiliou<sup>2</sup>

<sup>1</sup>*University of Campinas - UNICAMP,*

*Institute of Physics “Gleb Wataghin”, 13083-859 Campinas, SP, Brazil*

<sup>2</sup>*Department of Theoretical Physics and IFIC, University of Valencia and CSIC,  
E-46100, Valencia, Spain*

## Abstract

We determine the non-Abelian version of the four non-transverse form factors of the quark-gluon vertex, using exact expressions derived from the Slavnov-Taylor identity that this vertex satisfies. In addition to the quark and ghost propagators, a key ingredient of the present approach is the quark-ghost scattering kernel, which is computed within the one-loop dressed approximation. The vertex form factors obtained from this procedure are evaluated for arbitrary Euclidean momenta, and display features not captured by the well-known Ball-Chiu vertex, deduced from the Abelian (ghost-free) Ward identity. Particularly interesting in this analysis is the so-called soft gluon limit, which, unlike other kinematic configurations considered, is especially sensitive to the approximations employed for the vertex entering in the quark-ghost scattering kernel, and may even be affected by a subtle numerical instability. As an elementary application of the results obtained, we evaluate and compare certain renormalization-point-independent combinations, which contribute to the interaction kernels appearing in the standard quark gap and Bethe-Salpeter equations. In doing so, even though all form factors of the quark-gluon vertex, and in particular the transverse ones which are unconstrained by our procedure, enter non-trivially in the aforementioned kernels, only the contribution of a single form factor, corresponding to the classical (tree-level) tensor, will be considered.

PACS numbers: 12.38.Aw, 12.38.Lg, 14.70.Dj

## I. INTRODUCTION

Despite the fact that the quark-gluon vertex,  $\Gamma_\mu^a$ , has been the focal point of countless theoretical and phenomenological studies that span at least two decades, a complete understanding of its structure and properties still eludes us. Given the central role that this particular vertex plays in some of the most important nonperturbative phenomena of QCD, such as dynamical chiral symmetry breaking, the generation of constituent quark masses [1–5], and the formation of bound states [6–15], its systematic scrutiny constitutes one of the main challenges of contemporary hadron physics. In fact, the level of complexity may require the skillful combination of ingredients obtained from diverse approaches and frameworks, such as Schwinger-Dyson equations (SDEs) [8, 10, 14–23], gauge-technique inspired Ansätze [21, 24–33], functional renormalization group [34, 35], and lattice simulations [36–43], before a fully satisfactory nonperturbative picture could emerge<sup>1</sup>.

In the linear covariant ( $R_\xi$ ) gauges, the full vertex  $\Gamma_\mu^a(q, p_2, -p_1)$ , when contracted by the gluon momentum  $q^\mu$ , satisfies a non-linear Slavnov-Taylor identity (STI), imposed by the Becchi-Rouet-Stora-Tyutin (BRST) symmetry of the theory. This STI is the non-Abelian equivalent of the QED Ward-Takahashi identity (WTI),  $q^\mu \Gamma_\mu(q, p_2, -p_1) = S_e^{-1}(p_1) - S_e^{-1}(p_2)$ , which relates the photon-electron vertex with the electron propagator  $S_e$ . The non-Abelian nature of the STI manifests itself through the presence of multiplicative contributions originating from the ghost-sector of the theory, and in particular the “ghost dressing function”,  $F(q^2)$ , and the “quark-ghost scattering kernel”,  $H$ , together with its “conjugate”,  $\overline{H}$ .

Exactly as happens with the QED vertex, the Lorentz decomposition of  $\Gamma_\mu^a$  consists of twelve linearly independent tensorial structures, which are most conveniently expressed in the well-known Ball-Chiu (BC) basis [31]; the corresponding form factors are functions of three kinematic variables, *e.g.*, the moduli of  $p_1$  and  $p_2$ , and their relative angle  $\theta$ . The actual form of the BC basis is inspired by the aforementioned STI, being explicitly separated into two distinct pieces: (i) the “*non-transverse part*”, which saturates the STI, and is composed of four tensors that are not annihilated upon contraction by  $q^\mu$ , and (ii) the purely “*transverse*” (automatically conserved) part, which is composed of the remaining eight elements of the BC basis, all of which vanish identically when contracted by  $q^\mu$ .

---

<sup>1</sup> In perturbation theory, a complete study has been carried out at the one- and two-loop level in arbitrary linear covariant gauges, dimensions and kinematics in Refs. [44] and [45] respectively. In addition, Refs. [46–48] contain results at the one-, two- and three-loop order for specific gauges and kinematic limits.

Evidently, the STI imposes stringent constraints on the non-transverse form factors, denoted by  $L_1$ ,  $L_2$ ,  $L_3$ , and  $L_4$ ; in fact, as has been demonstrated in detail in [4], these four quantities are *fully determined* in terms of closed formulas involving the components of  $S$ ,  $F$ ,  $H$ , and  $\overline{H}$ . In the Abelian limit, *i.e.*, when the ghost-related contributions are set to their tree-level values, these expressions reduce to the known “BC vertex”, with the corresponding form factors denoted by  $L_1^{\text{BC}}$ ,  $L_2^{\text{BC}}$ ,  $L_3^{\text{BC}}$ , and  $L_4^{\text{BC}}$  (note that they depend only on the moduli of  $p_1$  and  $p_2$ , and that  $L_4^{\text{BC}}$  vanishes identically). The BC vertex has been extensively employed in the literature, both in QED, where it captures the non-transverse part of the photon-electron vertex exactly, as well as in QCD, where it is clearly approximate, but serves as a starting point towards a systematic improvement over the rainbow-ladder truncation [2]. Instead, the approach put forth in [4] permits, at least in principle, the complete *non-Abelian* conversion of the BC vertex, namely the reconstruction of the part of  $\Gamma_\mu^a$  that satisfies the *exact* STI, as dictated by the BRST symmetry.

The practical implementation of this particular approach requires the evaluation of  $H$  and  $\overline{H}$  by means of their own dynamical equations, rather than the more cumbersome treatment of the typical SDE that controls the dynamics of the form factors of  $\Gamma_\mu^a$ . The equations that govern  $H$  and  $\overline{H}$  are also of the SDE-type, but, unlike the vertex SDE, their one-loop dressed approximation involves a single Feynman diagram. Actually, a considerable simplification stems from the fact that the three-gluon vertex, a well-known source of technical complexity, does not appear in this particular diagram, and becomes relevant only at the next order of the loop expansion. Even so, the dependence of  $H$  and  $\overline{H}$  on three kinematic variables has been a limiting factor in the numerical treatment presented in [4], where only certain special kinematic configurations, involving a single momentum variable, were considered (see also [22] for a related study).

In the present work we compute the general form of  $L_1$ ,  $L_2$ ,  $L_3$ , and  $L_4$  by evaluating the one-loop dressed version of the dynamical equations for the components of  $H$  and  $\overline{H}$ , for arbitrary Euclidean momenta, in the *Landau gauge*. These equations contain the following main ingredients: (a) the gluon propagator,  $\Delta(q^2)$ ; (b) the ghost propagator,  $D(q^2)$  or, equivalently, its dressing function,  $F(q^2)$ ; (c) the two standard Dirac components of the quark propagator,  $A(q^2)$  and  $B(q^2)$ , introduced in Eq. (2.4); (d) the full ghost-gluon vertex and the full quark-gluon vertex  $\Gamma_\mu^a$ , both nested inside the one-loop dressed diagram.

Ideally, the above quantities ought to be determined self-consistently from their own

dynamical equations, which would be solved simultaneously together with the equations determining  $H$  and  $\overline{H}$ , thus forming an extended system of coupled integral equations. However, given the complexity of such an endeavor, in the present work we have opted for a simpler procedure. In particular, for the Landau gauge  $\Delta(q^2)$  and  $F(q^2)$  we use directly the results of the large-volume lattice simulations of [49], whereas two different sets of  $A(q^2)$  and  $B(q^2)$  are obtained from the solution of two standard forms of the quark gap equation in the same gauge. The main ingredients composing the kernels of these gap equations are again the aforementioned lattice results for the  $\Delta(q^2)$  and  $F(q^2)$ , with judicious modeling of the  $\Gamma_\mu^a$  entering in them. As far as the one-loop dressed diagram describing  $H$  is concerned, we will use for the internal propagators again the same  $\Delta(q^2)$  and  $F(q^2)$ , for the ghost-gluon vertex its tree-level expression, while for the  $\Gamma_\mu^a$  we will only keep its component of  $L_1^{\text{BC}}$ .

The main results obtained from our analysis may be briefly summarized as follows.

1. All four form factors are finite within the entire range of Euclidean momenta.
2.  $L_1$  displays a smoother and more enhanced structure compared to  $L_1^{\text{BC}}$ .
3.  $L_2$  has a rather intricate structure, whose details depend strongly on the particular shape of  $A(p^2)$ , but is, in general, considerably different from  $L_2^{\text{BC}}$ .
4.  $L_3$  exhibits practically the same qualitative behavior as its BC counterpart, with mild differences in the deep infrared.
5.  $L_4$  is non-vanishing but extremely suppressed in the entire range of momenta, with its maximum value being only  $0.027 \text{ GeV}^{-1}$ .
6. In general, the dependence of  $L_2$ ,  $L_3$ , and  $L_4$  on the angle  $\theta = 0$  is rather mild;  $L_1$  is also rather insensitive to changes in  $\theta$ . However, when  $\theta = 0$  and  $p_1 = p_2$ , it develops a more intricate behavior which requires a delicate analysis. In that sense, the form factors obtained depend mainly on the moduli of  $p_1$  and  $p_2$ , exactly as happens with their BC counterparts, even though their corresponding functional dependences are in general different.
7. For all values of  $\theta$ ,  $L_2$ ,  $L_3$ , and  $L_4$  suffers only quantitative changes when the Ansatz for the quark-gluon vertex entering in the calculation of the quark-ghost scattering

kernel is modified;  $L_1$ , is also quite insensitive to the Ansatz chosen, except when  $\theta = 0$  and  $p_1 = p_2$ , where a particularly strong dependence is observed.

We end this introductory section by emphasizing that the method presented here, being a variant of the “gauge-technique” [24–27], leaves the “transverse” part of the vertex completely undetermined. The proper inclusion of this part in SDE studies is essential because it enforces the multiplicative renormalizability of the electron and quark gap equations [4, 28–30]. Moreover, it affects considerably the amount of dynamical chiral symmetry breaking obtained [50], and is involved in the dynamics of various emerging nonperturbative phenomena [8, 10, 14, 16, 35, 51, 52]. Even though the transverse part is only partially determined by the so-called “transverse” WTI [53–58], a recent detailed study reveals that the imposition of certain crucial physical requirements severely restricts its allowed form and strength [59].

The article is organized as follows. In section II we introduce the notation and set up the theoretical framework of this work. In section III we derive the equations that govern the behavior of the form factors of  $H$  for arbitrary momenta, and discuss certain phenomenological subtleties related with the choice of the non-transverse basis for the quark gluon vertex. Our main results are presented in section IV, where we first obtain the numerical solution for the various  $X_i$  for general values of the Euclidean momenta, and then determine the quark-gluon form factors which satisfies the *exact* STI for arbitrary momenta. A considerable part of our study focuses on the dependence of the  $L_i$  on the value of the quark mass, and the shape (presence or absence of minimum) of the inverse quark wave functions. In section V we take a closer look at the form factors  $L_i$  in five special kinematic configurations. We pay particular attention to the case of the soft-gluon limit, whose numerical evaluations appears to be particularly delicate, and, even though subjected to an extensive number of checks, may still contain a certain amount of imprecision. In section VII we use some of the results derived in the previous section in order to construct certain renormalization-group invariant (RGI) combinations that serve as natural candidates for describing the effective strength of the quark interaction. Finally, in section VIII we draw our conclusions, and in the Appendix A present the Taylor expansions needed in the derivation of the special kinematic limits discussed in the section V.

## II. GENERAL FRAMEWORK

In this section we set up the notation and conventions that will be employed throughout this article, and review the general theoretical framework together with the fundamental equations that will be central to our subsequent analysis.

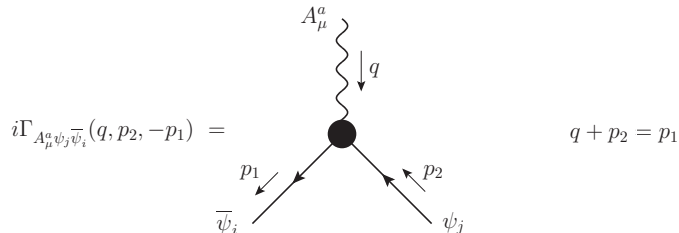


FIG. 1. The full quark-gluon vertex and the flow of momenta we employ.

Our starting point is the definition of the quark-gluon vertex, shown in Fig. 1, written as

$$\Gamma_{\mu}^a(q, p_2, -p_1) = gt^a \Gamma_{\mu}(q, p_2, -p_1), \quad (2.1)$$

where  $t^a = \lambda^a/2$  are the  $SU(3)$  group generators in the fundamental representation, with  $\lambda^a$  the Gell-Mann matrices,  $q$  and  $p_2$  are the incoming gluon and quark momenta,  $p_1 = q + p_2$  is the outgoing anti-quark momentum. At tree level, the vertex reduces to  $\Gamma_{\mu}^{[0]}(q, p_2, -p_1) = \gamma_{\mu}$ .

In addition,  $\Gamma_{\mu}$  satisfies the standard STI given by

$$q^{\mu} \Gamma_{\mu}(q, p_2, -p_1) = F(q^2) [S^{-1}(p_1)H(q, p_2, -p_1) - \overline{H}(-q, p_1, -p_2)S^{-1}(p_2)], \quad (2.2)$$

where  $F(q^2)$  is the ghost dressing function appearing in the definition of the complete ghost propagator

$$D(q^2) = \frac{iF(q^2)}{q^2}, \quad (2.3)$$

and  $S^{-1}(p)$  is the inverse of the full quark propagator expressed as

$$S^{-1}(p) = A(p^2)\not{p} - B(p^2), \quad (2.4)$$

where  $A(p^2)$  is the inverse of the quark wave function and  $B(p^2)$  is the scalar component (mass function) of the quark propagator, and  $\mathcal{M}(p^2) = B(p^2)/A(p^2)$  is the dynamically generated quark constituent mass. Finally,  $H$  denotes the quark-ghost scattering kernel, and  $\overline{H}$  its “conjugate”, represented diagrammatically in the Fig. 2.

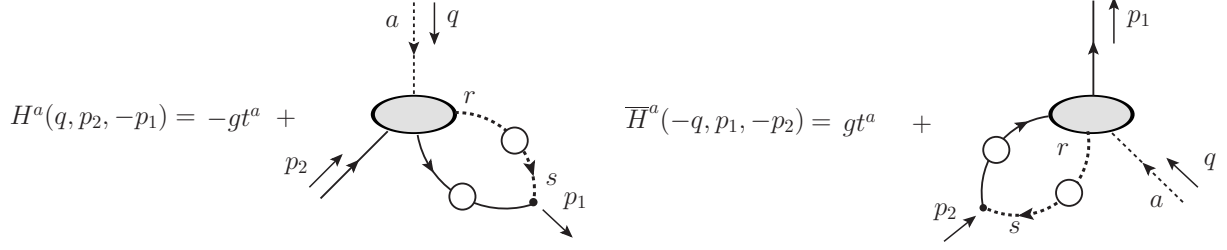


FIG. 2. Diagrammatic representation of the quark-ghost kernels  $H$  and  $\overline{H}$ ; their tree-level expressions are  $-gt^a$  and  $gt^a$ , respectively. The gray oval-shaped blob represents the *connected part* of the four-point quark-ghost scattering amplitude.

Turning to these last two quantities, notice that  $\overline{H}$  may be obtained from  $H$  through the application of the following operations: (i) exchange  $-p_1$  with  $p_2$ :  $-p_1 \leftrightarrow p_2$ ; (ii) reverse the sign of all external momenta:  $q, -p_1, p_2 \leftrightarrow -q, p_1, -p_2$ ; (iii) take the hermitian conjugate of the resulting amplitude, and use that

$$\overline{H} := \gamma^0 H^\dagger \gamma^0. \quad (2.5)$$

The Lorentz decomposition of  $H(q, p_2, -p_1)$  is given by [44]

$$H = X_0(q^2, p_2^2, p_1^2)\mathbb{I} + X_1(q^2, p_2^2, p_1^2)\not{p}_1 + X_2(q^2, p_2^2, p_1^2)\not{p}_2 + X_3(q^2, p_2^2, p_1^2)\tilde{\sigma}_{\mu\nu}p_1^\mu p_2^\nu, \quad (2.6)$$

where  $\tilde{\sigma}_{\mu\nu} = \frac{1}{2}[\gamma_\mu, \gamma_\nu]$  (notice the  $i$  difference with respect to the conventional definition of this quantity). At tree-level,  $X_0^{(0)} = 1$  and  $X_1^{(0)} = X_2^{(0)} = X_3^{(0)} = 0$ , while the complete one-loop expressions have been presented in [44].

The corresponding decomposition for  $\overline{H}$  may be easily deduced from Eq. (2.6) through the direct application of the aforementioned operations (i)–(iii), using subsequently Eq. (2.5). Thus, given that  $(\gamma^\mu)^\dagger = \gamma^0 \gamma^\mu \gamma^0$  and  $\tilde{\sigma}_{\mu\nu}^\dagger = \gamma^0 \tilde{\sigma}_{\nu\mu} \gamma^0$ , one obtains that  $\overline{H}(-q, p_1, -p_2)$

$$\overline{H} = X_0(q^2, p_1^2, p_2^2)\mathbb{I} + X_2(q^2, p_1^2, p_2^2)\not{p}_1 + X_1(q^2, p_1^2, p_2^2)\not{p}_2 + X_3(q^2, p_1^2, p_2^2)\tilde{\sigma}_{\mu\nu}p_1^\mu p_2^\nu. \quad (2.7)$$

For the sake of notational compactness, in what follows we will employ the definitions

$$X_i := X_i(q^2, p_2^2, p_1^2), \quad \overline{X}_i := X_i(q^2, p_1^2, p_2^2). \quad (2.8)$$

On the other hand, the tensorial structure of the full quark-gluon vertex,  $\Gamma_\mu$ , consists of 12 independent vectors [31]. It is common to divide the vertex into a part that “saturates”

the STI of Eq. (2.2), denoted here by  $\Gamma_\mu^{(\text{ST})}$ , and a ‘‘transverse part’’, denoted by  $\Gamma_\mu^{(\text{T})}$  which is automatically conserved,

$$q^\mu \Gamma_\mu^{(\text{T})}(q, p_2, -p_1) = 0. \quad (2.9)$$

Thus,

$$\Gamma_\mu(q, p_2, -p_1) = \Gamma_\mu^{(\text{ST})}(q, p_2, -p_1) + \Gamma_\mu^{(\text{T})}(q, p_2, -p_1). \quad (2.10)$$

Evidently, the above decomposition is not unique, given that a ‘‘transverse’’ structure may be removed from  $\Gamma_\mu^{(\text{T})}$  and be reassigned to  $\Gamma_\mu^{(\text{ST})}$ . This ambiguity introduces a corresponding arbitrariness at the level of the tensorial basis used to span  $\Gamma_\mu^{(\text{ST})}(q, p_2, -p_1)$  and  $\Gamma_\mu^{(\text{T})}(q, p_2, -p_1)$ . One of the most standard choices for the decomposition of the ST part, is the so-called BC basis [31], given by

$$\Gamma_\mu^{(\text{ST})}(q, p_2, -p_1) = \sum_{i=1}^4 L_i(q, p_2, -p_1) \lambda_{i,\mu}(p_1, p_2), \quad (2.11)$$

with

$$\begin{aligned} \lambda_{1,\mu} &= \gamma_\mu, \\ \lambda_{2,\mu} &= (\not{p}_1 + \not{p}_2)(p_1 + p_2)_\mu, \\ \lambda_{3,\mu} &= (p_1 + p_2)_\mu, \\ \lambda_{4,\mu} &= \tilde{\sigma}_{\mu\nu}(p_1 + p_2)^\nu, \end{aligned} \quad (2.12)$$

where  $L_i(q, p_2, -p_1)$  are the form factors.

For the transverse part,  $\Gamma_\mu^{(\text{T})}$ , one may use the basis proposed in Ref. [60]

$$\Gamma_\mu^{(\text{T})}(q, p_2, -p_1) = \sum_{i=1}^8 T_i(q, p_2, -p_1) \tau_{i,\mu}(p_1, p_2), \quad (2.13)$$

where  $T_i(q, p_2, -p_1)$  are the form factors and the set of independent tensors  $\tau_i$  are given by

$$\begin{aligned} \tau_{1,\mu} &= p_{2\mu}(p_1 \cdot q) - p_{1\mu}(p_2 \cdot q); & \tau_{2,\mu} &= \tau_{1\mu} \not{t}; \\ \tau_{3,\mu} &= q^2 \gamma_\mu - q_\mu \not{q}; & \tau_{4,\mu} &= q^2 [\gamma_\mu \not{t} - t_\mu] - 2q_\mu \tilde{\sigma}_{\nu\lambda} p_1^\nu p_2^\lambda; \\ \tau_{5,\mu} &= \tilde{\sigma}_{\mu\nu} q^\nu; & \tau_{6,\mu} &= \gamma_\mu (q \cdot t) - t_\mu \not{q}; \\ \tau_{7,\mu} &= \frac{1}{2} (q \cdot t) \lambda_{4,\mu} - t_\mu \tilde{\sigma}_{\nu\lambda} p_1^\nu p_2^\lambda; & \tau_{8,\mu} &= \gamma_\mu \tilde{\sigma}_{\nu\lambda} p_1^\nu p_2^\lambda + p_{2\mu} \not{p}_1 - p_{1\mu} \not{p}_2, \end{aligned} \quad (2.14)$$

with  $q = p_1 - p_2$  and  $t = p_1 + p_2$ . Note that Eq. (2.14) not only explicitly satisfies Eq. (2.9), but also guarantees that  $\tau_{i,\mu}(p_1, p_1) = 0$ .

It is important to mention that the above decomposition for  $\Gamma_\mu^{(T)}(q, p_2, -p_1)$  is slightly different from the one first employed by Ball-Chiu [31]. The modification, proposed in Ref. [60] guarantees that the corresponding form factors are free of kinematic singularities in all covariant gauges [46, 60]. In addition, this basis also permits one to establish a more transparent relation between the ST and the transverse parts of the vertex. More specifically, when we contract the tensors defining the ST part with the transverse projector,  $P_{\mu\nu}(q) = g_{\mu\nu} - \frac{q_\mu q_\nu}{q^2}$ , we obtain [37]

$$\begin{aligned} P_{\mu\nu}(q)\lambda_1^\nu &= \frac{1}{q^2}\tau_{3,\mu}; & P_{\mu\nu}(q)\lambda_2^\nu &= \frac{2}{q^2}\tau_{2,\mu}; \\ P_{\mu\nu}(q)\lambda_3^\nu &= \frac{2}{q^2}\tau_{1,\mu}; & P_{\mu\nu}(q)\lambda_4^\nu &= \frac{1}{q^2}\tau_{4,\mu}. \end{aligned} \quad (2.15)$$

which clearly shows that  $\Gamma_\mu^{(ST)}$  contains transverse contributions, or else the above contractions would have vanished.

It is interesting to notice that Eq. (2.15) has a great impact on the applications of the quark-gluon vertex in the study of chiral symmetry breaking and the formation of bound states. To see that, we recall that in the dynamical equations describing both phenomena, one of the relevant quantities appearing on them is the contraction of the full quark-gluon vertex with the transverse projector, namely  $P_\mu^\nu(q)\Gamma_\nu(q, p_2, -p_1)$  [see for example Fig. 22 of the section VII]. Using Eqs. (2.9), (2.10), and (2.15) we conclude that the aforementioned contraction will produce

$$\begin{aligned} P_\mu^\nu(q)\Gamma_\nu(q, p_2, -p_1) &= P_\mu^\nu(q)\Gamma_\nu^{(ST)}(q, p_2, -p_1) + \Gamma_\mu^{(T)}(q, p_2, -p_1) \\ &= \frac{1}{q^2}[L'_1\tau_{3,\mu}(p_1, p_2) + 2L'_2\tau_{2,\mu}(p_1, p_2) + 2L'_3\tau_{1,\mu}(p_1, p_2) + L'_4\tau_{4,\mu}(p_1, p_2)] \\ &\quad + \sum_{i=5}^8 T_i\tau_{i,\mu}(p_1, p_2), \end{aligned} \quad (2.16)$$

where the form factors  $L_i$  get entangled with the  $T_i$ , generating the following modified (effective) form factors [37]

$$\begin{aligned} L'_1 &= L_1 + q^2 T_3; & L'_2 &= L_2 + \frac{q^2}{2} T_2; \\ L'_3 &= L_3 + \frac{q^2}{2} T_1; & L'_4 &= L_4 + q^2 T_4. \end{aligned} \quad (2.17)$$

It is important to emphasize at this point that, if we had chosen a basis different from that of Eqs. (2.12) and (2.14), the above relations would be modified. In fact, as far as

phenomenological applications are concerned (such as those discussed in section VII), an appropriate choice of basis is necessary in order to profitably exploit the information encoded in the STI.

In order to appreciate this point with a concrete example, let us assume that the basis given in (2.12) is modified by changing  $\lambda_{1,\mu}$  to  $\bar{\lambda}_{1,\mu}$  through the addition of a transverse piece, *i.e.*, ,

$$\bar{\lambda}_{1,\mu} = \gamma_\mu + cP_{\mu\nu}(q)\gamma^\nu = \left( (1+c)g_{\mu\nu} - c\frac{q_\mu q_\nu}{q^2} \right) \gamma^\nu, \quad (2.18)$$

where  $c$  is an arbitrary real number. Clearly, in this new basis, the tree level quark-gluon vertex is decomposed as

$$\Gamma_\mu^{[0]} = \bar{\lambda}_{1,\mu} - \frac{c}{q^2}\tau_{3,\mu}. \quad (2.19)$$

Now, given that the difference between  $\lambda_{1,\mu}$  and  $\bar{\lambda}_{1,\mu}$  is a purely transverse piece, the change of basis is not felt at the level of the STI; therefore, the form factors  $L_1$  and  $\bar{L}_1$  will be identical,  $L_1 = \bar{L}_1$ . On the other hand, the first projection given in Eq. (2.15) becomes  $c$ -dependent, since now

$$P_{\mu\nu}(q)\bar{\lambda}_1^\nu = \frac{1+c}{q^2}\tau_{3,\mu}, \quad (2.20)$$

while the first relation of Eq. (2.17) becomes

$$L'_1 = (1+c)L_1 + q^2T_3, \quad (2.21)$$

revealing that, indeed, the answer of the transversely projected vertex depends on the details of the basis chosen for the  $\Gamma_\mu^{(\text{ST})}$  part. In fact, for the special value  $c = -1$ , for which  $\bar{\lambda}_{1,\mu} = q_\mu \not{q}/q^2$ , all information furnished by the STI (namely the form of  $L_1$ ), is completely washed out from the corresponding amplitude. The above argument may be easily generalized to all remaining elements of the basis that spans  $\Gamma_\mu^{(\text{ST})}$ .

There are two main conclusions that may be drawn from the discussion presented above. First, a necessary condition for exploiting the STI in phenomenological applications is that the basis used for  $\Gamma_\mu^{(\text{ST})}$  should *not* be completely annihilated when contracted by the transverse projector. Second, the amount of  $L_i$  that enters into the amplitude (in other words, the value of “ $c$ ” in the case of  $L_1$ ) *depends on the basis* chosen for  $\Gamma_\mu^{(\text{ST})}$ ; we will consider this issue again in section VII.

Returning to Eq. (2.11), it is clear that the form factors  $L_i$  can be related through Eq. (2.2) with  $A$ ,  $B$ ,  $F$ ,  $X_i$ , and  $\bar{X}_i$ . Specifically, as was demonstrated in [4], the  $L_i$  may be expressed

as

$$\begin{aligned}
L_1 &= \frac{F(q)}{2} \{A(p_1)[X_0 - (p_1^2 + p_1 \cdot p_2)X_3] + A(p_2)[\bar{X}_0 - (p_2^2 + p_1 \cdot p_2)\bar{X}_3]\} \\
&\quad + \frac{F(q)}{2} \{B(p_1)(X_2 - X_1) + B(p_2)(\bar{X}_2 - \bar{X}_1)\}; \\
L_2 &= \frac{F(q)}{2(p_1^2 - p_2^2)} \{A(p_1)[X_0 + (p_1^2 - p_1 \cdot p_2)X_3] - A(p_2)[\bar{X}_0 + (p_2^2 - p_1 \cdot p_2)\bar{X}_3]\} \\
&\quad - \frac{F(q)}{2(p_1^2 - p_2^2)} \{B(p_1)(X_1 + X_2) - B(p_2)(\bar{X}_1 + \bar{X}_2)\}; \\
L_3 &= \frac{F(q)}{p_1^2 - p_2^2} \{A(p_1)(p_1^2 X_1 + p_1 \cdot p_2 X_2) - A(p_2)(p_2^2 \bar{X}_1 + p_1 \cdot p_2 \bar{X}_2) - B(p_1)X_0 + B(p_2)\bar{X}_0\}; \\
L_4 &= \frac{F(q)}{2} \{A(p_1)X_2 - A(p_2)\bar{X}_2 - B(p_1)X_3 + B(p_2)\bar{X}_3\}. \tag{2.22}
\end{aligned}$$

The derivation of the above equation has been carried out in Minkowski space; its Euclidean version may be obtained through direct application of the rules given in the subsection III A.

Setting in Eq. (2.22)  $X_0 = \bar{X}_0 = 1$  and  $X_i = \bar{X}_i = 0$ , for  $i \geq 1$ , and  $F(q) = 1$ , we obtain the following expressions (still in Minkowski space)

$$\begin{aligned}
L_1^{\text{BC}} &= \frac{A(p_1) + A(p_2)}{2}, & L_2^{\text{BC}} &= \frac{A(p_1) - A(p_2)}{2(p_1^2 - p_2^2)}, \\
L_3^{\text{BC}} &= \frac{B(p_2) - B(p_1)}{p_1^2 - p_2^2}, & L_4^{\text{BC}} &= 0. \tag{2.23}
\end{aligned}$$

which is precisely the well-known BC vertex [31].

### III. QUARK-GHOST KERNEL AT THE ONE-LOOP DRESSED LEVEL

In this section we derive the expressions for the form factors  $X_i$  within the one-loop dressed approximation. In particular, the four-point quark-ghost scattering amplitude, entering in the diagrammatic definition of  $H^a = -gt^a H$  in Fig. 2, is approximated by its lowest order diagram, the one gluon exchange term, which is subsequently ‘‘dressed’’ as shown in Fig. 3.

Using the flow of momenta defined in Fig. 3 and factoring out its color structure ( $-gt^a$ ), the expression for  $H^{[1]}(q, p_2, -p_1)$  is given by

$$H^{[1]} = 1 - \frac{1}{2} i C_A g^2 \int_l \Delta^{\mu\nu}(l - p_2) G_\nu(p_1 - l) D(l - p_1) S(l) \Gamma_\mu(l - p_2, p_2, -l), \tag{3.1}$$

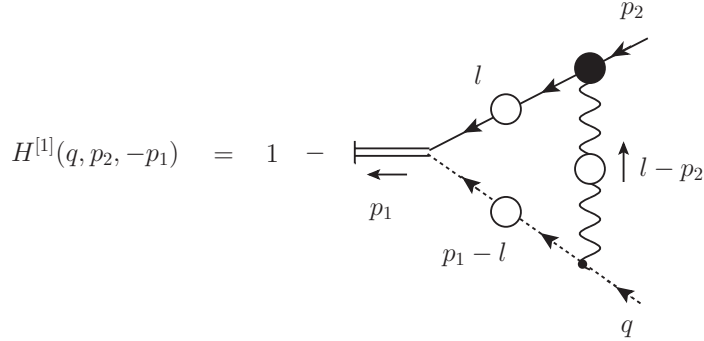


FIG. 3. The scattering kernel  $H^{[1]}(q, p_2, -p_1)$  at one-loop dressed approximation.

where we have already used the three level expression for the the quark-ghost kernel,  $H^{[0]a} = -gt^a$ , as indicated in the Fig. 2. In addition,  $C_A$  is the eigenvalue of the Casimir operator in the adjoint representation and we have defined the integration measure

$$\int_l \equiv \int \frac{d^4l}{(2\pi)^4}; \quad (3.2)$$

it is understood that a symmetry preserving regularization scheme must be employed (see also subsection VB). In addition,  $\Delta^{\mu\nu}(k)$  is the full gluon propagator, which in the Landau gauge has the form

$$\Delta_{\mu\nu}(k) = -iP_{\mu\nu}(k)\Delta(k^2), \quad P_{\mu\nu}(k) = g_{\mu\nu} - \frac{k_\mu k_\nu}{k^2}. \quad (3.3)$$

In order to evaluate Eq. (3.1) further, we will use for the full gluon-ghost vertex its tree-level value<sup>2</sup>, *i.e.*,  $G_\nu^{abc} = -gf^{abc}(p_1 - l)_\nu$ .

The question of how to approximate the  $\Gamma_\mu$  that enters in  $H^{[1]}$  turns out to be particularly subtle. Evidently, if one were to consider only the non-transverse part of this vertex (as we do throughout this work), the most complete treatment would entail to replace the  $\Gamma_\mu$  by the  $\Gamma_\mu^{(\text{ST})}$  of Eq. (2.11), using the  $L_i$  given in Eq. (2.22). This choice, however, would convert the problem into a system of coupled integral equations for the  $L_i$ , whose solution, unfortunately, lies beyond our present powers. Instead, we will reduce the level of technical complexity by employing a simpler expression for  $\Gamma_\mu$ , retaining only the component proportional to  $\gamma_\mu$ , and approximating its form factor  $L_1$  using tree-level values for the  $X_i$  entering in it. With

<sup>2</sup> Evidently, a more detailed analysis along the lines of the Ref. [22] should be eventually performed, in order to establish the numerical impact of this approximation.

these simplifications, one has

$$\Gamma_\mu(l - p_2, p_2, -l) = \frac{F(l - p_2)}{2} [A(l) + A(p_2)] \gamma_\mu. \quad (3.4)$$

However, as we will discuss in section IV C, the use of this particular expression leads to unnatural results for the form factor corresponding to the soft gluon kinematics: essentially, the curve reverses sign, and deviates dramatically from the expected perturbative behavior in the ultraviolet. Interestingly enough, the expected ultraviolet behavior is restored if instead of (3.4) one uses

$$\Gamma_\mu(l - p_2, p_2, -l) = \frac{1}{2} [A(l) + A(p_2)] \gamma_\mu, \quad (3.5)$$

which is simply  $L_1^{\text{BC}}(l - p_2, p_2, -l)$ .

It seems therefore that, depending on the kinematic circumstances, the presence of the ghost dressing function  $F(l - p_2)$  in this particular part of the calculation destabilizes the truncation procedure. In what follows we will present the results obtained using Eq. (3.5) for all kinematic configurations other than that of the soft gluon limit; we have checked explicitly that, for all these cases, the use of Eq. (3.4) does not affect the answers appreciably, and, in that sense, our results are rather stable. Instead, for the special case of the soft gluon configuration, we will show the results obtained with both Eqs. (3.4) and (3.5) (see the panels of Fig. 8 and Fig. 19), in order to fully appreciate the difference between the two.

Then, we proceed inserting into Eq. (3.1) the propagators of Eqs. (2.4) and (3.3) together with the Ansatz given by Eq. (3.5), it is straightforward to derive the following expression for  $H$

$$H(q, p_2, -p_1) = 1 + \frac{i}{4} C_A g^2 \int_l \mathcal{K}(p_1, p_2, l) f(p_2, q, l), \quad (3.6)$$

where we have introduced the kernel

$$\mathcal{K}(p_1, p_2, l) = \frac{F(l - p_1) \Delta(l - p_2) [A(l) + A(p_2)]}{(l - p_1)^2 [A^2(l) l^2 - B^2(l)]}, \quad (3.7)$$

with

$$f(p_2, q, l) = A(l) \left[ l \not{q} - q \cdot (l - p_2) \left( 1 + \frac{(\not{p}_2 l - p_2^2)}{(l - p_2)^2} \right) \right] + B(l) \left[ \not{q} - (l - \not{p}_2) \frac{q \cdot (l - p_2)}{(l - p_2)^2} \right]. \quad (3.8)$$

Notice that if we had used the Ansatz given by Eq. (3.4) instead of Eq. (3.5), the unique difference in the derivation was that the kernel of Eq. (3.7) would be replaced by  $\mathcal{K}(p_1, p_2, l) \rightarrow F(l - p_2)\mathcal{K}(p_1, p_2, l)$ .

The next step is to project out of Eq. (3.6) the individual form factors  $X_i$ . This is easily accomplished by means of the following formulas [4]

$$\begin{aligned} X_0 &= \frac{\text{Tr}\{H\}}{4}, \\ X_1 &= \frac{p_2^2 \text{Tr}\{\not{p}_1 H\} - p_1 \cdot p_2 \text{Tr}\{\not{p}_2 H\}}{4h}, \\ X_2 &= \frac{p_1^2 \text{Tr}\{\not{p}_2 H\} - p_1 \cdot p_2 \text{Tr}\{\not{p}_1 H\}}{4h}, \\ X_3 &= -\frac{\text{Tr}\{\tilde{\sigma}_{\alpha\beta} p_1^\alpha p_2^\beta H\}}{4h}, \end{aligned} \quad (3.9)$$

where we have introduced the function

$$h = p_1^2 p_2^2 - (p_1 \cdot p_2)^2, \quad (3.10)$$

and the arguments of  $X_i$  have been suppressed as before.

After substituting the Eq. (3.6) into the projectors given by Eqs. (3.9) and taking the appropriate traces, we obtain

$$\begin{aligned} X_0 &= 1 + \frac{i}{4} C_A g^2 \int_l \mathcal{K}(p_1, p_2, l) A(l) \mathcal{G}(p_2, q, l), \\ X_1 &= \frac{i}{4} C_A g^2 \int_l \frac{\mathcal{K}(p_1, p_2, l) B(l)}{h(p_1, p_2)} [p_2^2 \mathcal{G}(p_1, q, l) - (p_1 \cdot p_2) \mathcal{G}(p_2, q, l)], \\ X_2 &= \frac{i}{4} C_A g^2 \int_l \frac{\mathcal{K}(p_1, p_2, l) B(l)}{h(p_1, p_2)} [p_1^2 \mathcal{G}(p_2, q, l) - (p_1 \cdot p_2) \mathcal{G}(p_1, q, l)], \\ X_3 &= -\frac{i}{4} C_A g^2 \int_l \frac{\mathcal{K}(p_1, p_2, l) A(l)}{h(p_1, p_2)} [p_2^2 \mathcal{G}(p_1, q, l) - (p_1 \cdot p_2) \mathcal{G}(p_2, q, l) - \mathcal{T}(p_1, p_2, l)], \end{aligned} \quad (3.11)$$

where we have introduced the functions

$$\begin{aligned} \mathcal{G}(k, q, l) &= (k \cdot q) - \frac{[k \cdot (l - p_2)][q \cdot (l - p_2)]}{(l - p_2)^2}, \\ \mathcal{T}(p_1, p_2, l) &= (p_2 \cdot q)[(p_1 \cdot l) - (p_1 \cdot p_2)] - (p_1 \cdot q)[(p_2 \cdot l) - p_2^2]. \end{aligned} \quad (3.12)$$

### A. Passing to the Euclidean space

Next, we will convert the Eq. (3.11) from Minkowski to Euclidean space. To do that we will employ the following transformation rules, which are valid for two arbitrary momenta

$p$  and  $q$

$$(\not{p}, \not{q}) \rightarrow i(\not{p}_E, \not{q}_E); \quad (p^2, q^2, p \cdot q) \rightarrow -(p_E^2, q_E^2, p_E \cdot q_E). \quad (3.13)$$

In addition, the measure defined in Eq. (3.2) becomes

$$d^4l \rightarrow i d^4l_E, \quad \int_l \rightarrow i \int_{l_E}, \quad (3.14)$$

where we have introduced the Euclidean measure in spherical coordinates,

$$\int_{l_E} = \frac{1}{(2\pi)^4} \int d^4l = \frac{1}{32\pi^4} \int_0^\infty dl_E^2 l_E^2 \int_0^\pi d\varphi_1 \sin^2 \varphi_1 \int_0^\pi d\varphi_2 \sin \varphi_2 \int_0^{2\pi} d\varphi_3. \quad (3.15)$$

Applying the above rules to the scalar functions appearing in the definition of the various propagators, lead us to the following relations

$$\begin{aligned} A_E(p_E^2) &= A(-p^2); & B_E(p_E^2) &= B(-p^2); \\ \Delta_E(q_E^2) &= -\Delta(-q^2); & F_E(q_E^2) &= F(-q^2). \end{aligned} \quad (3.16)$$

Then, it is straightforward to see that, after applying the conversion rules defined in the Eqs. (3.13) and (3.16), the quantities appearing in Eq. (3.11) transform in the following way

$$\begin{aligned} \mathcal{K}(p_1^2, p_2^2, l^2) &\rightarrow -\mathcal{K}_E(-p_{1E}^2, -p_{2E}^2, -l_E^2), \\ \mathcal{G}(k^2, q^2, l^2) &\rightarrow -\mathcal{G}_E(-k_E^2, -q_E^2, -l_E^2), \\ \mathcal{T}(p_1^2, p_2^2, l^2) &\rightarrow \mathcal{T}_E(-p_{1E}^2, -p_{2E}^2, -l_E^2). \end{aligned} \quad (3.17)$$

In order to avoid notational clutter, from now on we will suppress the subscript  $E$ .

Then, we can easily see that, in a general kinematic configuration, the various form factors  $X_i$  and  $L_i$  are expressed in terms of the Euclidean scalar products  $(p_1 \cdot p_2)$ ,  $(p_1 \cdot l)$ , and  $(p_2 \cdot l)$ . Without loss of generality, a convenient choice for Euclidean four momenta  $p_1$  and  $p_2$  is

$$p_1^\mu = |p_1| \begin{pmatrix} \cos \theta \\ \sin \theta \\ 0 \\ 0 \end{pmatrix}, \quad p_2^\mu = |p_2| \begin{pmatrix} 1 \\ 0 \\ 0 \\ 0 \end{pmatrix}, \quad (3.18)$$

where  $|p_1|$  and  $|p_2|$  are the magnitudes of the Euclidean momenta and  $\theta$  is the angle between them. Notice that the above choices guarantee that  $(p_1 \cdot p_1) = p_1^2$  and  $(p_2 \cdot p_2) = p_2^2$ .

Similarly, the integration momentum  $l$  can be written as

$$l^\mu = |l| \begin{pmatrix} \cos \varphi_1 \\ \sin \varphi_1 \cos \varphi_2 \\ \sin \varphi_1 \sin \varphi_2 \cos \varphi_3 \\ \sin \varphi_1 \sin \varphi_2 \sin \varphi_3 \end{pmatrix}. \quad (3.19)$$

With the above definitions, it is evident that the Euclidean scalar products  $(p_1 \cdot p_2)$ ,  $(p_1 \cdot l)$ , and  $(p_2 \cdot l)$ , appearing in the Euclidean version of the Eq. (3.11), do not display any dependence on the angle  $\varphi_3$ , so that the integral over this angle becomes trivial, and the measure may be cast in the form

$$\int_{l_E} = \frac{1}{(2\pi)^4} \int d^4 l = \frac{1}{16\pi^3} \int_0^\infty dl^2 l^2 \int_0^\pi d\varphi_1 \sin^2 \varphi_1 \int_0^\pi d\varphi_2 \sin \varphi_2. \quad (3.20)$$

Finally, the Euclidean form of Eq. (3.11) becomes

$$\begin{aligned} X_0(p_1, p_2, \theta) &= 1 + \frac{C_A g^2}{4} \int_{l_E} \frac{\mathcal{K}(p_1, p_2, l) A(l^2)}{s^2} \{ p_2^2 l^2 \sin^2 \varphi_1 - s^2 p_1 p_2 \cos \theta \\ &\quad + [p_1 l (\cos \theta \cos \varphi_1 + \sin \theta \sin \varphi_1 \cos \varphi_2) - p_1 p_2 \cos \theta] (p_2 l \cos \varphi_1 - p_2^2) \}, \\ X_1(p_1, p_2, \theta) &= \frac{C_A g^2}{4} \int_{l_E} \frac{\mathcal{K}(p_1, p_2, l) B(l^2)}{s^2} \left[ s^2 - l^2 \sin^2 \varphi_1 \cos^2 \varphi_2 \right. \\ &\quad \left. + l (l \cos \varphi_1 - p_2) \left( \frac{p_2}{p_1} - \cos \theta \right) \frac{\sin \varphi_1 \cos \varphi_2}{\sin \theta} \right], \\ X_2(p_1, p_2, \theta) &= \frac{C_A g^2}{4} \int_{l_E} \frac{\mathcal{K}(p_1, p_2, l) B(l^2)}{s^2} \left[ (l \cos \varphi_1 - p_2)^2 \left( 1 - \frac{p_1}{p_2} \cos \theta \right) - s^2 \right. \\ &\quad \left. + \frac{p_1 l^2}{p_2} \cos \theta \sin^2 \varphi_1 \cos^2 \varphi_2 - \frac{p_1 l}{p_2} (l \cos \varphi_1 - p_2) \sin \theta \sin \varphi_1 \cos \varphi_2 \right. \\ &\quad \left. - l (l \cos \varphi_1 - p_2) \cos \theta \left( 1 - \frac{p_1}{p_2} \cos \theta \right) \frac{\sin \varphi_1 \cos \varphi_2}{\sin \theta} \right], \\ X_3(p_1, p_2, \theta) &= \frac{C_A g^2}{4} \int_{l_E} \frac{\mathcal{K}(p_1, p_2, l) A(l^2)}{s^2} \left[ -s^2 \frac{l \sin \varphi_1 \cos \varphi_2}{p_1 \sin \theta} \right. \\ &\quad \left. + s^2 \frac{l}{p_2} \left( \frac{\cos \theta \sin \varphi_1 \cos \varphi_2}{\sin \theta} - \cos \varphi_1 \right) \right. \\ &\quad \left. + l^2 \sin^2 \varphi_1 \cos^2 \varphi_2 + l (l \cos \varphi_1 - p_2) \left( \cos \theta - \frac{p_2}{p_1} \right) \frac{\sin \varphi_1 \cos \varphi_2}{\sin \theta} \right], \quad (3.21) \end{aligned}$$

where, in order to simplify the notation, we have defined  $p_1 \equiv |p_1|$ ,  $p_2 \equiv |p_2|$ ,  $l \equiv |l|$ , and the variable  $s^2 = l^2 + p_2^2 - 2lp_2 \cos \varphi_1$ .

Note that the functional dependence of the functions  $X_i$ , in Euclidean space, will be expressed in terms of the moduli of the momenta  $p_1$ ,  $p_2$ , and their relative angle  $\theta$ , as denoted by Eq. (3.21).

#### IV. RESULTS FOR GENERAL MOMENTA: 3-D PLOTS

In this section we will determine numerically the form factors  $X_i$  given by Eq. (3.21) for general values of the Euclidean momenta. All results will be presented in the form of 3-D plots<sup>3</sup>, where  $p_1$  and  $p_2$  will be varied, for fixed values of the angle  $\theta$ . The culmination of this analysis is presented at the final step, where the numerical solution obtained for the various  $X_i$  are fed into the Euclidean version of Eq. (2.22), giving rise to all quark-gluon form factors  $L_i$  for arbitrary momenta.

##### A. Inputs for the numerical analysis

The first step in this analysis is to consider the ingredients entering into the evaluation of the form factors  $X_i$  and the corresponding  $L_i$ . The computation of the  $X_i$  and  $L_i$ , in a general kinematic configuration, not only require the knowledge of the nonperturbative behavior of the gluon,  $\Delta(q^2)$ , and ghost,  $D(q^2)$ , propagators (or equivalently the ghost dressing function,  $F$ ), but the functions  $A(k^2)$  and  $B(k^2)$ , appearing in the decomposition of the full quark propagator of Eq. (2.4), see for example Eqs. (3.21) and (2.22).

Employing the same methodology of previous works [61–63], we use for  $\Delta$  and  $F$  a fit for the  $SU(3)$  lattice data of the Ref. [49]. In Fig. 4 we show the lattice data for  $\Delta(q^2)$  and  $F(q^2)$  and their corresponding fits, renormalized at  $\mu = 4.3$  GeV. The explicit functional dependence of  $\Delta(q^2)$  and  $F(q^2)$  may be found in a series of recent articles [4, 61, 63], and their main characteristic is the saturation in the deep infrared, associated with the generation of a dynamical gluon mass [64, 65].

---

<sup>3</sup> Throughout this work, all 3-D numerical data will be generically written as an array  $\mathcal{G}(p_1, p_2, \theta)$  with dimensions (96,96,7), *i.e.* we compute the function  $\mathcal{G}$  for 96 different values for each momentum  $p_1$  and  $p_2$  and 7 distinct values for the angle  $\theta$ . Then, all 3-D plots were produced using the Renka-Cline interpolation on the grid.

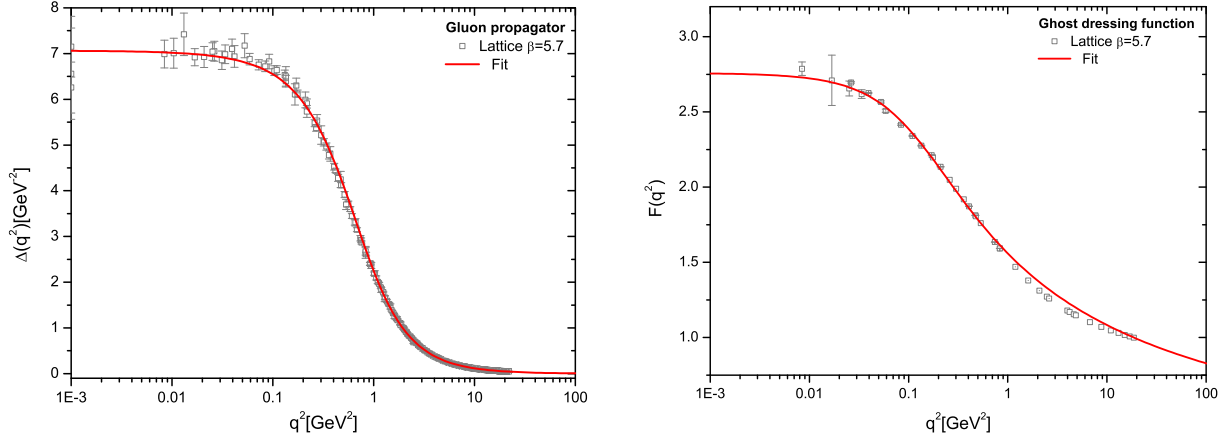


FIG. 4. The gluon propagator  $\Delta(q^2)$  (left panel) and the ghost dressing function  $F(q^2)$  (right panel), both renormalized at  $\mu = 4.3 \text{ GeV}$ . The lattice data is from Ref. [49].

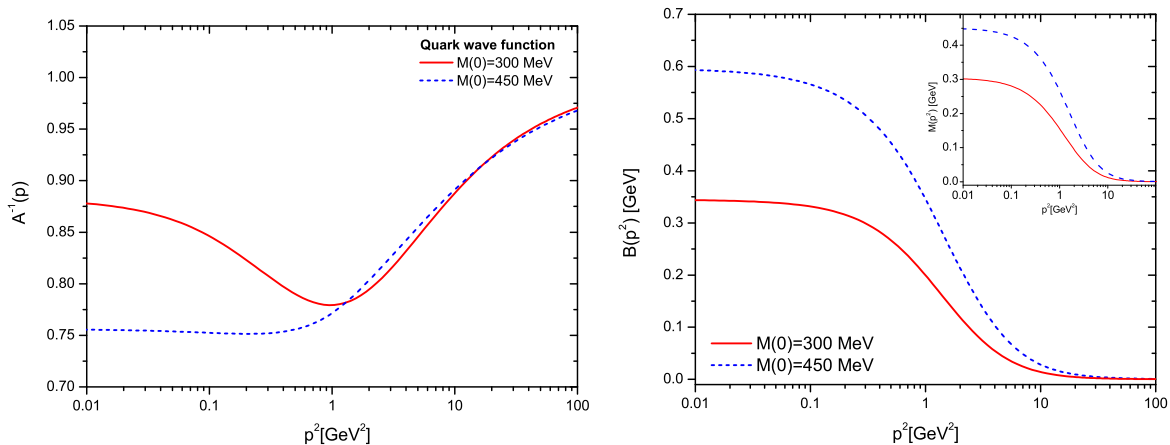


FIG. 5. The inverse quark wave function,  $A^{-1}(p^2)$ , (left panel) and the scalar component of the quark propagator,  $B(p^2)$  (right panel). In the inset we show the corresponding dynamical quark masses  $\mathcal{M}(p^2) = B(p^2)/A(p^2)$ .

The ingredients originating from the quark sector of the theory, namely  $A(k^2)$  and  $B(k^2)$ , will be obtained from two different versions of the quark gap equation: *(i)* the first one contains the BC vertex, endowed with the minimum amount of non-Abelian “dressing” necessary for achieving compliance with the renormalization group [see [4] and the discussion following Eq. (7.9)], and setting  $\alpha_s(\mu) = g^2(\mu)/4\pi = 0.28$ , *(ii)* the second one employs the Curtis-Pennington vertex [28], accompanied by a slightly enhanced non-Abelian dressing<sup>4</sup>,

<sup>4</sup> Specifically, in Eq. (7.9) one substitutes  $F(q^2)$  by  $[1 + G(q^2)]^{-1}$ ; a detailed discussion on the properties of the quantity  $1 + G(q^2)$ , and its relation to  $F(q^2)$ , may be found in [66].

and  $\alpha_s(\mu) = 0.29$ . The main practical difference between the two gap equations is that they produce qualitatively different forms of the quark wave function, and give rise to distinct constituent quark masses as are shown in Fig. 5. In particular, as has been recently pointed out in [59], the minimum displayed by  $A^{-1}(p^2)$  is intimately related to the values of  $\mathcal{M}(0)$ . Specifically,  $A^{-1}(p^2)$  maintains its minimum as long as the corresponding values for  $\mathcal{M}(0)$  are relatively low. But, when  $\mathcal{M}(0)$  exceeds a certain limiting value of approximately 350 MeV <sup>5</sup>, the aforementioned structure is practically eradicated. In order to explore the potential impact of this feature on the structure of the  $L_i$ , we have obtained a quark mass of  $\mathcal{M}(0) = 300$  MeV with an  $A^{-1}(p^2)$  with a rather pronounced minimum (red continuous line), and another of  $\mathcal{M}(0) = 450$  MeV, with an  $A^{-1}(p^2)$  whose minimum has disappeared (blue dashed line); note that the corresponding functions  $B(k^2)$  are monotonic in both cases.

Note that the  $A(p^2)$  and  $B(p^2)$  that give rise to a quark dynamical mass of  $\mathcal{M}(0) = 300$  MeV will be employed in the analysis presented in the subsections IV B, IV C and sections V and VII, whereas those producing  $\mathcal{M}(0) = 450$  MeV will be relevant for the subsection IV D.

Finally, it is important to stress that the inputs used in our calculations (gluon propagator and ghost dressing function) are quenched (no dynamical quarks). To be sure, the omission of quark effects while computing the quark-gluon vertex may seem a-priori conceptually inconsistent. However, the effects of “unquenching” have been found to be relatively small; in particular, the estimate provided in [32] for their relative impact is of the order of 10%.

## B. Form factors of the quark-ghost scattering kernel

At this point we have all ingredients and shall proceed to determine the various  $X_i$ , given by Eq. (3.21), for a general kinematic configuration. The main results and observations regarding the  $X_i$  obtained using a quark mass with  $\mathcal{M}(0) = 300$  MeV may be summarized as follows.

(i) In Fig. 6 the 3-D results for all  $X_i(p_1, p_2, 0)$  when  $\theta = 0$ . We observe that all  $X_i(p_1, p_2, 0)$  are finite in the infrared, and they recover the correct ultraviolet perturbative behavior. More specifically, in the limit of large momenta ( $p_1$  or  $p_2$ , or both) the 3-D curves tend to  $X_0 = 1$  and  $X_1 = X_2 = X_3 = 0$ .

---

<sup>5</sup> The actual value depends, among other things, on the structure and strength of the transverse part of the quark-gluon vertex that one uses.

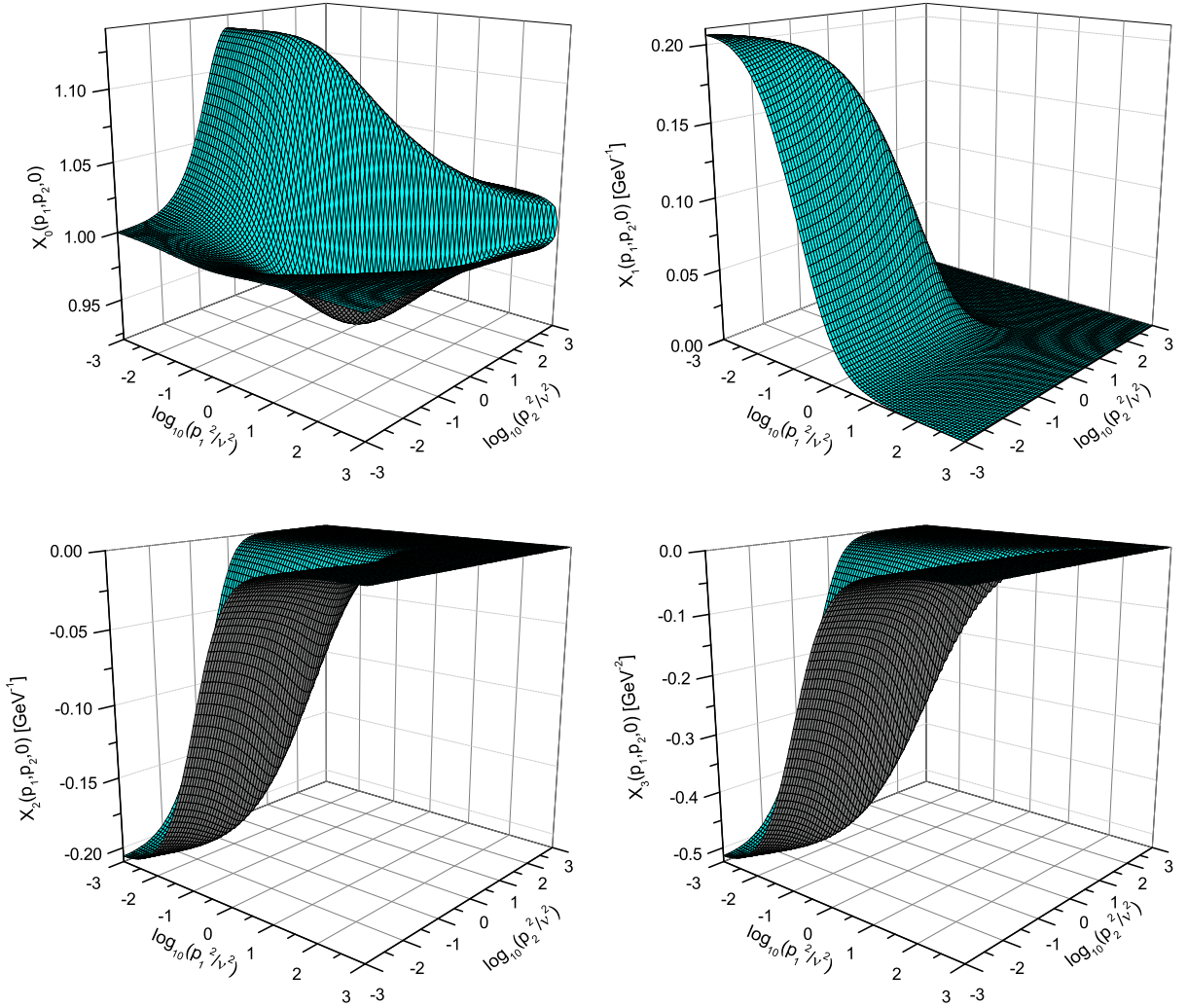


FIG. 6. The form factors  $X_i(p_1, p_2, 0)$  for an arbitrary kinematic configuration given by Eqs. (3.21) when  $\theta = 0$  and the scale parameter  $\nu = 1$  GeV.

(ii) From Fig. 6 we can infer the amount by which the  $X_i$  depart from their tree level values.  $X_0$  deviates 13% from its tree value, while for  $X_1$  and  $X_2$  the maximum deviation occurs at zero momenta scale, reaching the value of  $\pm 0.21$  GeV<sup>-1</sup>.  $X_3$  displays in the infrared region the maximum deviation value saturating at zero momenta around  $-0.52$  GeV<sup>-2</sup>. This last observation indicates that the impact of  $X_3$  on the quark-gluon vertex may be quite sizable.

(iii)  $X_0(p_1, p_2, 0)$  and  $X_1(p_1, p_2, 0)$  are positive definite for all values of  $p_1$  and  $p_2$ , whereas  $X_2(p_1, p_2, 0)$  and  $X_3(p_1, p_2, 0)$  are strictly negative within the entire range.

(iv) The direct comparison of the above form factors reveals that  $X_0(p_1, p_2, 0)$  displays

the richest structure, its main features being a pronounced “peak” and a shallow “well”. The peak has its maximum located in the infrared region, at  $p_1^2 = 0.009 \text{ GeV}^2$  and  $p_2^2 = 0.97 \text{ GeV}^2$ , whereas the well has its minimum around  $p_1^2 = 3.14 \text{ GeV}^2$  and  $p_2^2 = 0.97 \text{ GeV}^2$ .

(*v*) We have checked by analyzing a large number of cases that  $X_1$ ,  $X_2$  and  $X_3$  are quite insensitive to changes in the value of  $\theta$ , whereas  $X_0$  exhibits certain qualitative changes. More specifically, for the cases where  $\theta = \pi/2$  or  $\theta = \pi$ , the aforementioned “well” disappears.

As expected from Eq. (2.8), the conjugated form factors  $\overline{X}_i$ , in a general kinematic configuration, display exactly the same behavior shown in Fig. 6, and for this reason we will omit their explicit derivation here.

### C. Form factors of the quark-gluon vertex for $\mathcal{M}(0) = 300 \text{ MeV}$ .

With the  $X_i$  for general kinematic configurations at our disposal, we may now determine the behavior of the quark-gluon form factors  $L_i$  by means of Eq. (2.22).

Of course, the quark-gluon vertex, and in particular its component  $L_1$  (proportional to the tree-level vertex  $\gamma^\mu$ ), need to be properly renormalized. The renormalization is implemented as usual, through the introduction of the cutoff-dependent constant  $Z_1$ , namely

$$\Gamma_R^\nu(q, p_2, -p_1; \mu) = Z_1 \Gamma^\nu(q, p_2, -p_1). \quad (4.1)$$

The exact form of  $Z_1$  is determined within the momentum-subtraction (MOM) scheme, by imposing the condition that, at the totally symmetric point, *i.e.*, where all squared momenta are equal to the renormalization scale  $\mu^2$ , the quark-gluon vertex recovers its bare value, *i.e.*,

$$\Gamma^\mu(q, p_2, -p_1) \Big|_{p_1^2=p_2^2=q^2=\mu^2} = \gamma^\mu. \quad (4.2)$$

The results for  $L_1$ ,  $L_2$ ,  $L_3$ , and  $L_4$  are shown in Figs. 7, 9, 10, and 11, respectively. In each of these figures, we present the corresponding form factor for three representative values of the angle  $\theta$ , namely  $\theta = \pi/6$  (top left panels),  $\theta = \pi/3$  (top right panels), and  $\theta = \pi/2$  (bottom left panels). In order to facilitate a direct visual comparison, in the bottom right panels of these figures we plot the corresponding Abelian form factors,  $L_i^{\text{BC}}$ , given by Eq. (2.23), which, by construction, are independent of the angle  $\theta$ . The results for the individual form factors may be summarized as follows.

(*i*) From Fig. 7 it is clear that  $L_1$  displays a very mild dependence on  $\theta$ , except in the vicinity of  $\theta = 0$ , which, due to its particularity, is shown separately in Fig. 8. In this figure,

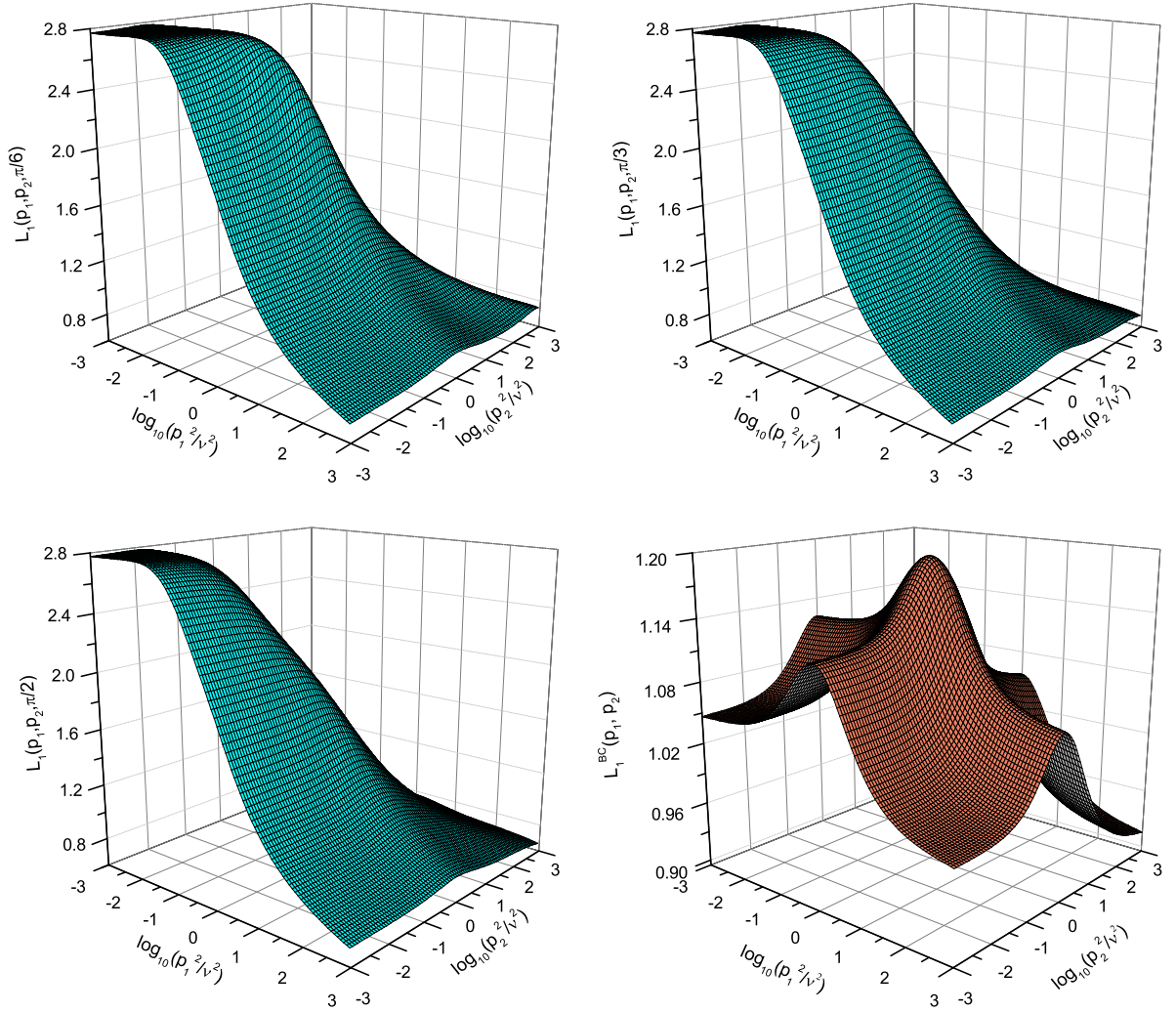


FIG. 7.  $L_1(p_1, p_2, \theta)$  for  $\theta = \pi/6$ ,  $\theta = \pi/3$ , and  $\theta = \pi/2$ . In the bottom right panel we show  $L_1^{\text{BC}}$  given by Eq. (2.23).

we clearly see that region located in the proximity of the slice defined by  $p_1 = p_2$  is drastically affected by the type of the quark-gluon vertex Ansatz we employ in the calculation of the various  $X_i$ . More specifically, the left panel shows  $L_1(p_1, p_2, 0)$  obtained with the Ansatz given by Eq. (3.5), whereas in the right panel we show the result obtained with the vertex of Eq. (3.4). The origin of the “slit” in the right panel of Fig. 8 can be traced back to the presence of an extra  $F(l-p_2)$  in the structure of the kernel of the Eq. (3.7) which is introduced by the Ansatz of Eq. (3.4). Notice that, only when  $p_1 = p_2$  (soft gluon limit), the arguments of both  $F$ , appearing in Eq. (3.7), become exactly the same. It is precisely the  $F^2(l-p_1)$  that causes steeper decrease observed in the right panel. Notice that, in the left panel, where

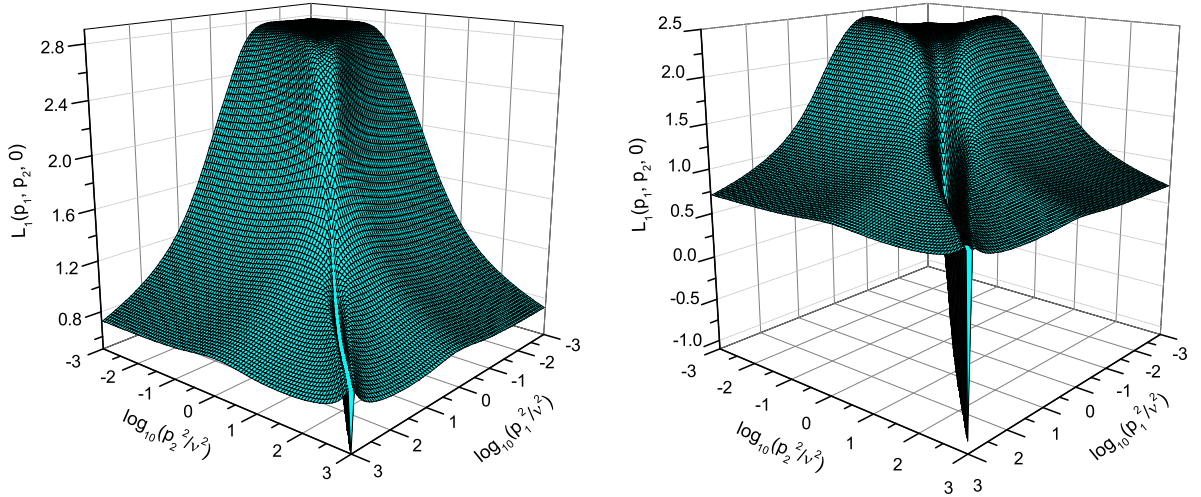


FIG. 8. The form factor  $L_1(p_1, p_2, 0)$  computed using either the Ansatz given by Eq. (3.5) (left panel) or the one of Eq. (3.4) (right panel). The plane defined by  $p_1 = p_2$  gives the result for the soft gluon configuration. Note that, in order to make the narrow “slit” more visible, we have rotated the plot with respect to Fig. 7, *i.e.*, the axes  $p_1$  and  $p_2$  have been interchanged.

the kernel of Eq. (3.7) counts with a unique  $F(l - p_1)$ , the “slit” is practically inexistent. We emphasize that, with the exception of  $L_1(p_1, p_2, 0)$ , all other  $L_1(p_1, p_2, \theta)$  display only small quantitative changes (smaller than 18%) when both Ansätze are employed. Even though, evidently, further future analysis related to this point is required, the sensitivity of  $L_1(p_1, p_2, 0)$  to the particular shape of the vertex employed, suggests that the tensorial structures omitted in both Ansätze given by Eq. (3.5) and Eq. (3.4) may play an important role for the complete elimination of the “slit” appearing in Fig. 8.

(*ii*) Turning to the  $L_2$  shown in Fig. 9, we note that it displays a slightly stronger dependence on  $\theta$  than  $L_1$ , which affects mainly the size of the peak located in the intermediate region of momenta. As we can see,  $L_2$  is one order of magnitude smaller compared to  $L_1$ . In addition, while  $L_2^{\text{BC}}$  is negative for all momenta,  $L_2$  contains some small positive regions (peaks). Moreover, they are clearly similar in the deep infrared region.

(*iii*) From Fig. 10 we infer that the angular dependence of  $L_3$  is very mild. In addition,  $L_3$  is always negative and tends to zero in the limit of large momenta (either  $p_1$  or  $p_2$ , or both). Moreover, we see that  $L_3$  reaches sizable values (in modulo) for values of  $p_1$  and  $p_2$  smaller than  $10^{-1} \text{ GeV}^2$ . As a final remark, we notice that although  $L_3^{\text{BC}}$  is more suppressed

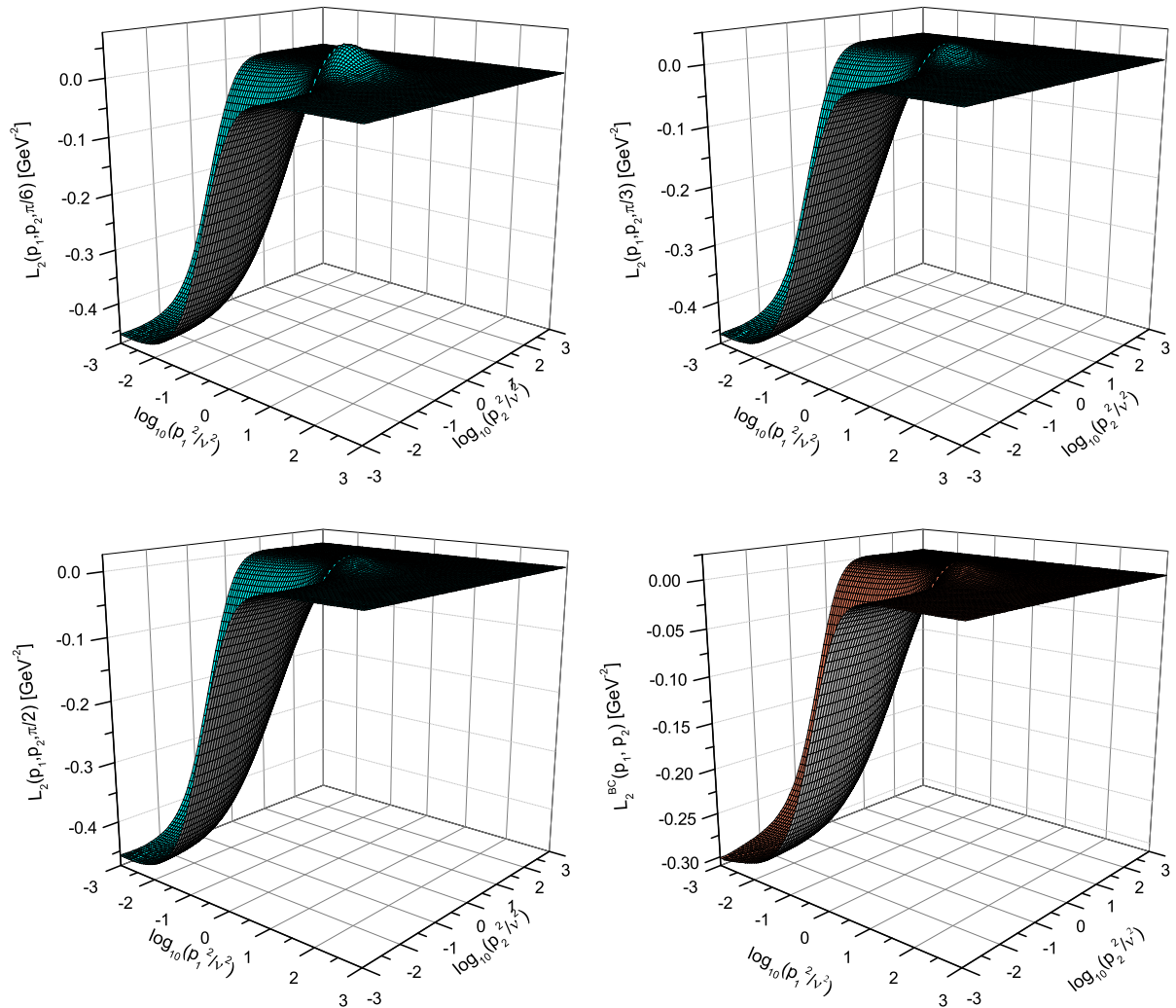


FIG. 9.  $L_2(p_1, p_2, \theta)$  for  $\theta = \pi/6$ ,  $\theta = \pi/3$ , and  $\theta = \pi/2$ , together with  $L_2^{\text{BC}}$  (bottom right panel).

than  $L_3$ , its shape is very similar to that of  $L_3$ ; the region of momenta where the difference is more pronounced is in deep infrared, where, unlike  $L_3$ , the  $L_3^{\text{BC}}$  displays a minimum.

(iv) As can be seen in Fig. 11, the angular dependence of  $L_4$  is essentially negligible, and the most prominent characteristic is its suppressed structure within the entire range of momenta, reaching a maximum value of at most  $0.027 \text{ GeV}^{-2}$ . We recall here that  $L_4^{\text{BC}}$  vanishes identically [see Eq. (2.23)].

(v) For later convenience, we show in the Fig. 12 the results for  $L_1$  when  $\theta = 2\pi/3$  (left panel) and  $\theta = \pi$  (right panel) which will be used to determine some special kinematic configurations.

(vi) Finally, in order to fully appreciate the numerical impact of the quark-ghost scatter-

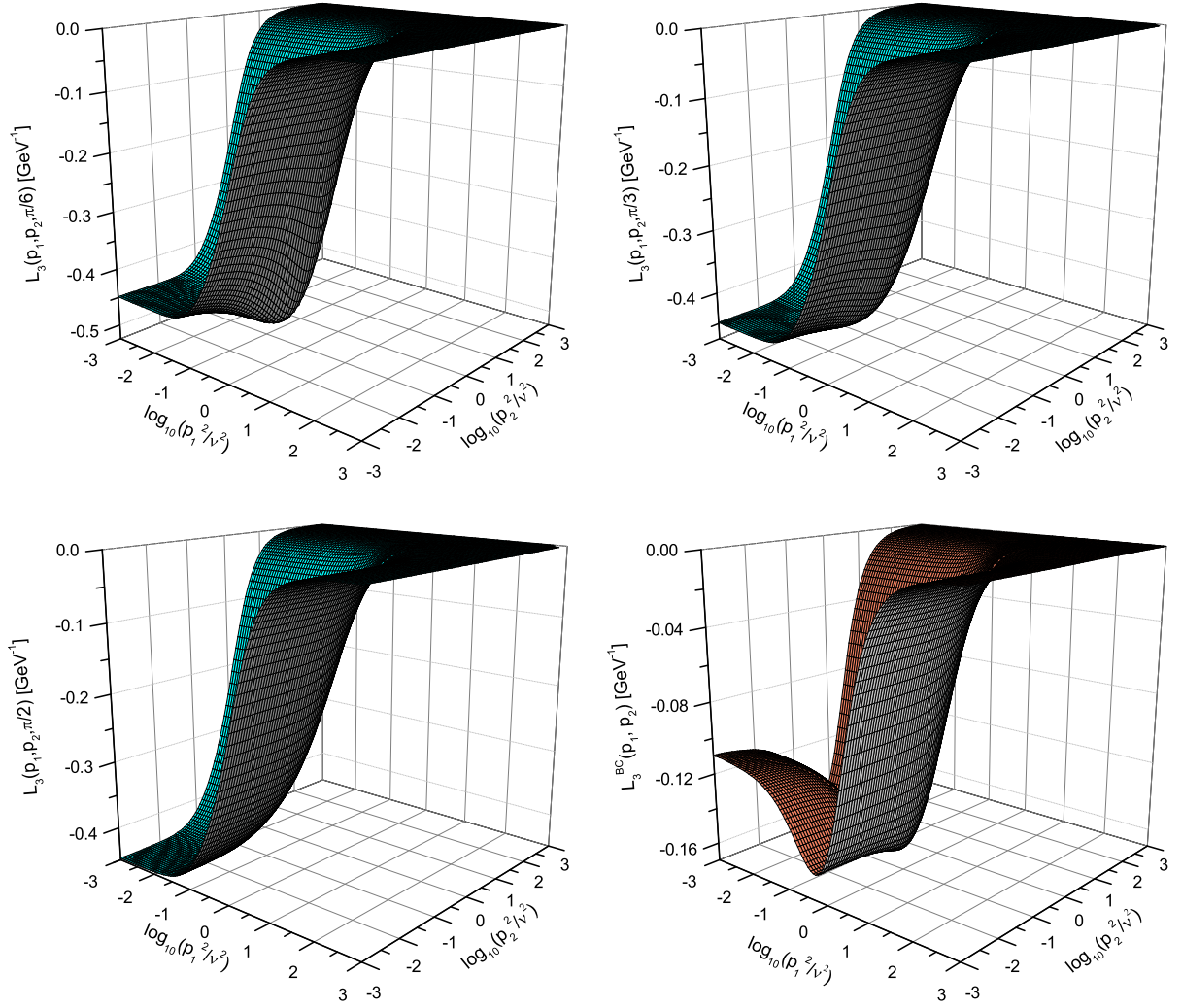


FIG. 10.  $L_3(p_1, p_2, \theta)$  for  $\theta = \pi/6$ ,  $\theta = \pi/3$ , and  $\theta = \pi/2$ , together with  $L_3^{\text{BC}}$  (bottom right panel).

ing kernel on the form factors  $L_i$ , in Fig. 13 we compare our results (colored surface) with those obtained when the quark-ghost scattering is fixed at its tree-level value (cyan surface) for a fixed angle ( $\theta = \pi/6$ ). More specifically, setting in Eq. (2.22)  $X_0 = \bar{X}_0 = 1$  and  $X_i = \bar{X}_i = 0$ , for  $i \geq 1$ , we obtain the “minimal” non-Abelian Ansatz for the quark-gluon vertex,  $F(q)L_i^{\text{BC}}$  [3, 4, 23]. In Fig. 13, we clearly see that our results for  $L_1$  and  $L_2$  (colored surface) are significantly more suppressed (in modulo) compared with those obtained with the “minimal” non-Abelian Ansatz (cyan surface). On the other hand, in the case of  $L_3$  we observe the opposite effect.

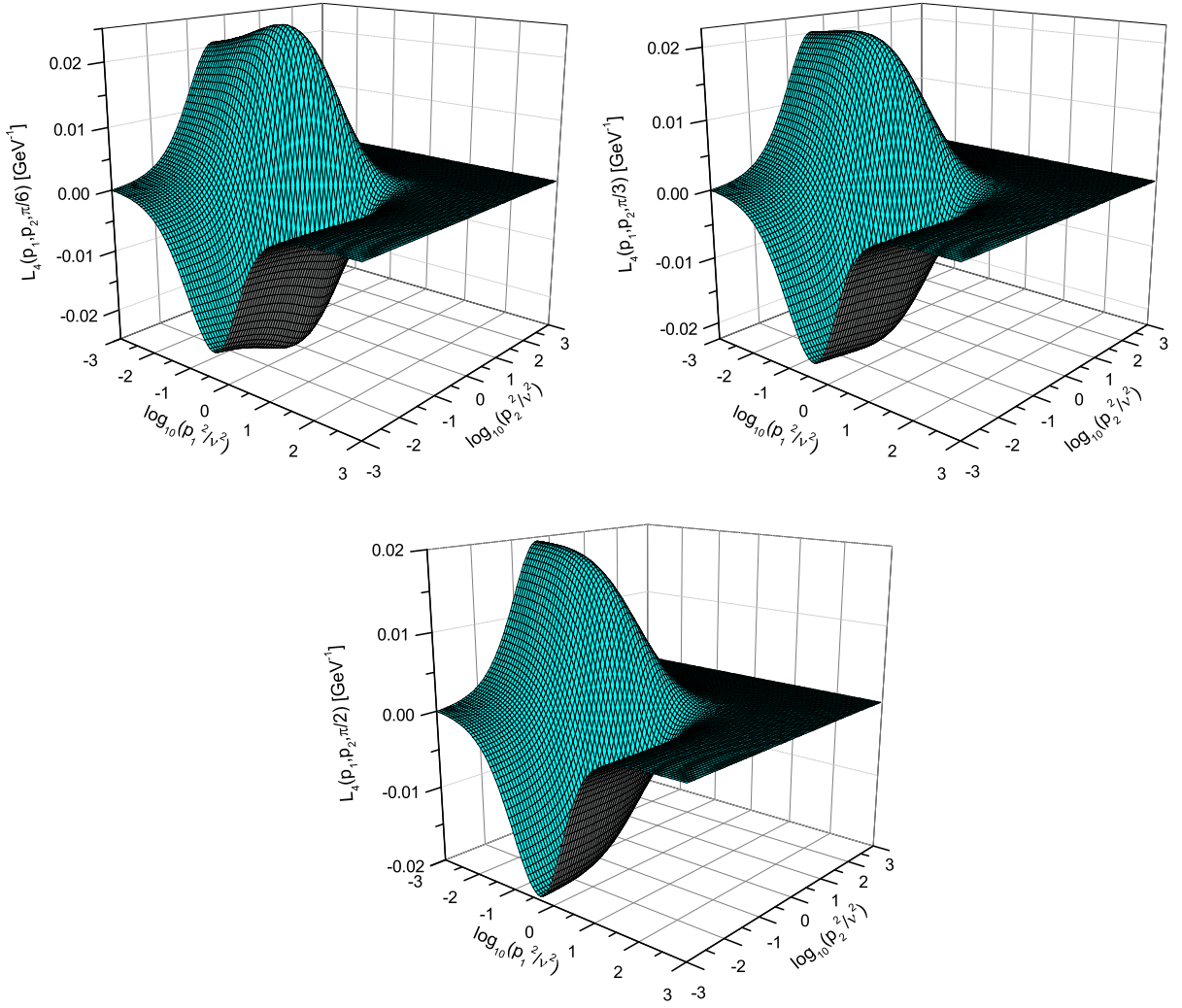


FIG. 11.  $L_4(p_1, p_2, \theta)$  for  $\theta = \pi/6$ ,  $\theta = \pi/3$ , and  $\theta = \pi/2$ . Note that  $L_4^{\text{BC}}$  vanishes identically.

#### D. Form factors of the quark-gluon vertex for $\mathcal{M}(0) = 450$ MeV.

We next analyze the differences that a higher value of the quark mass  $\mathcal{M}(p^2)$  and a nearly monotonic  $A(p^2)$  may produce in the overall shape of the  $L_i$ . To that end, we have recomputed the  $X_i$  and  $L_i$ , using as ingredients the  $A(p^2)$  and  $B(p^2)$  that give rise to  $\mathcal{M}(0) = 450$  MeV (see the blue-dashed line in Fig. 5).

It turns out that the qualitative behavior for all  $X_i$  are very similar to those already presented in the Fig. 6. More specifically, we notice that for  $X_0$ ,  $X_1$  and  $X_2$  the differences in their extrema are at most of the order of 10%. In the case of  $X_0$  the maximum of the curve changes from 1.13 to 1.11, whereas for  $X_1$  and  $X_2$  their extrema increase from  $\pm 0.20$   $\text{GeV}^{-1}$  to  $\pm 0.22$   $\text{GeV}^{-1}$  (see Fig. 6). On the other hand,  $X_3$  is the one which suffers the biggest

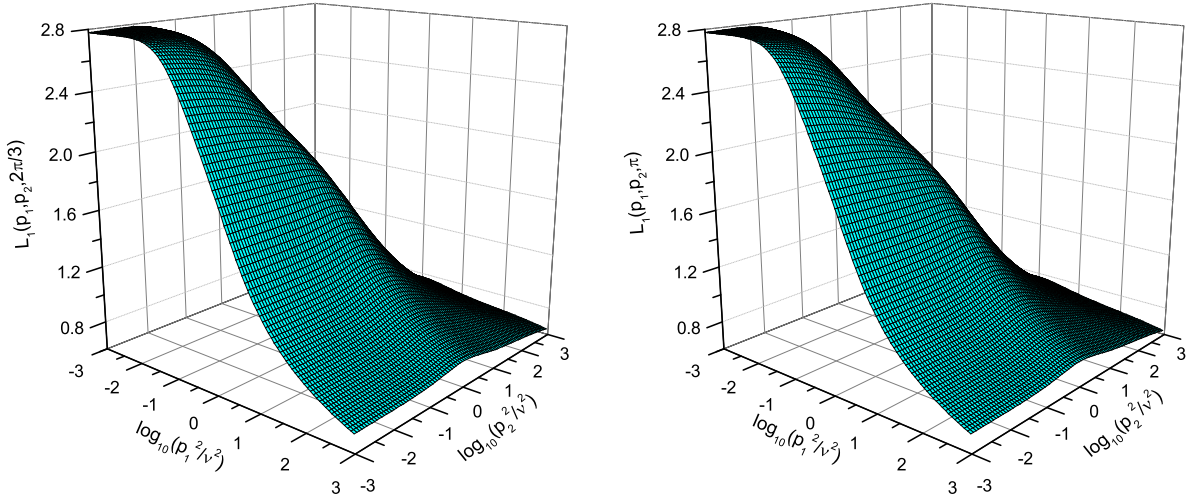


FIG. 12. The form factors  $L_1(p_1, p_2, \theta)$  for  $\theta = 2\pi/3$  (left panel) and  $\theta = \pi$  (right panel).

suppression ( $\approx 27.5\%$  in modulo), saturating now at  $-0.40 \text{ GeV}^{-2}$  instead of  $-0.51 \text{ GeV}^{-2}$ . Since the new set of  $X_i$  is qualitatively very similar to the previous one, we will omit the corresponding plots.

The next step is the determination of the  $L_i$  from Eq. (2.22); the results for  $\theta = \pi$  are shown in the left panels of Fig. 14 and 15. As before, in order to expose the non-Abelian content of these form factors, on the right panels we plot their Abelian counterparts,  $L_i^{BC}$ . Moreover, in Fig. 16 we show the result for  $L_4$  alone, since  $L_4^{BC} = 0$ . The comparison of the results in Figs. 14, 15 and 16 with those presented previously in the sequence of Figs. 7, 9, 10, and 11, allows us to make the following remarks.

(i) The results for  $L_1$ ,  $L_3$  and  $L_4$  are qualitatively rather similar, and do not seem especially sensitive to the particular shape of  $A(p^2)$  and  $B(p^2)$ , nor to the amount of dynamical quark mass generated.

(ii) Instead,  $L_2$  changes completely its shape in the infrared, displaying a structure which is not so smoother compared to that of Fig. 9. We notice that, when  $A(p^2)$  is nearly monotonic in the infrared,  $L_2$  reverses its sign and becomes positive in the entire range of momenta, saturating in the infrared around  $0.1 \text{ GeV}^{-2}$  [see left bottom panel of Figs. 14]. This rather abrupt change may be traced back to the fact that,  $A(p^2)$  enters in the expression for  $L_2$  multiplied by a particular combination of  $X_0$  and  $X_3$  [see Eq. (2.22)]; in the limit of  $p_1 \rightarrow p_2$ , this combination reduces to a derivative-like term. Since the corrections of

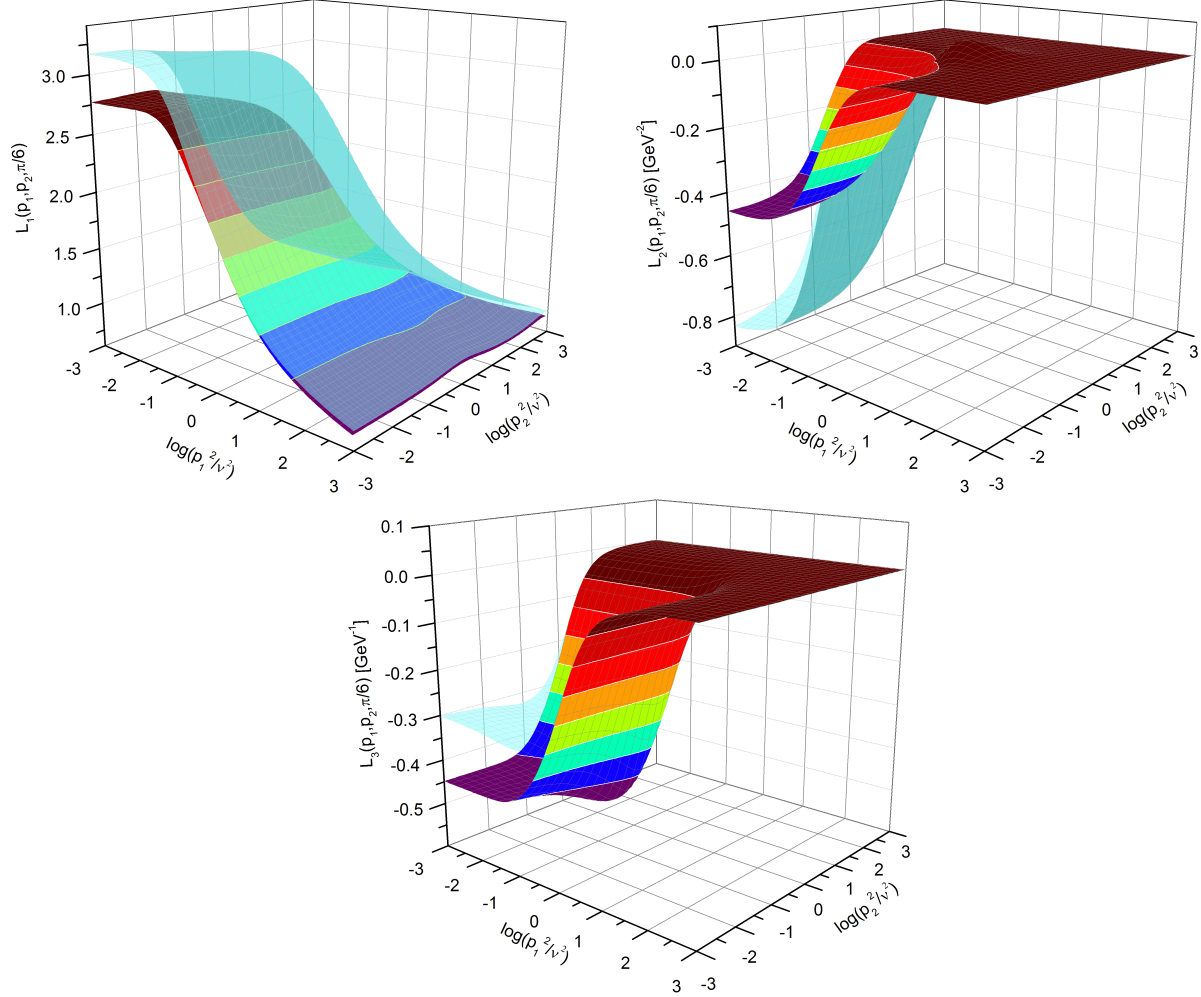


FIG. 13. Comparison of the form factors  $L_i(p_1, p_2, \theta)$  (colored surface) with the “minimal” non-Abelian Ansatz,  $F(q)L_i^{BC}$  (cyan surface) for  $\theta = \pi/6$ .

both  $X_0$  and  $X_3$  are of the same order, any change in their infrared values may lead to an oscillation in the sign of  $L_2$ . It is interesting to notice that  $L_3$  also contains a similar term [see Eq. (2.22)]; however, in this case, the  $A(p^2)$  is multiplied by a combination of  $X_1$  and  $X_2$ , which tends to be very small in the infrared region, furnishing a subleading contribution to the overall shape of  $L_3$ .

(iii) Finally, as one might have intuitively expected, the Abelian form factors  $L_i^{BC}$  are significantly more sensitive to the precise functional forms of  $A(p^2)$  and  $B(p^2)$ . In particular, we notice that  $L_1^{BC}$  of Fig. 14 displays a much smoother behavior when compared with the one plotted in Fig. 7. Evidently, this is a direct consequence of having switched to a nearly

monotonic  $A(p^2)$ , since the planes where either  $p_1 = 0$  or  $p_2 = 0$  in the  $L_1^{BC}$  of Fig. 14 should reproduce (by construction) the same functional form of  $A(p^2)$  but shifted and multiplied by a constant, *i.e.*  $A(p^2)/2 + A(0)/2$ .

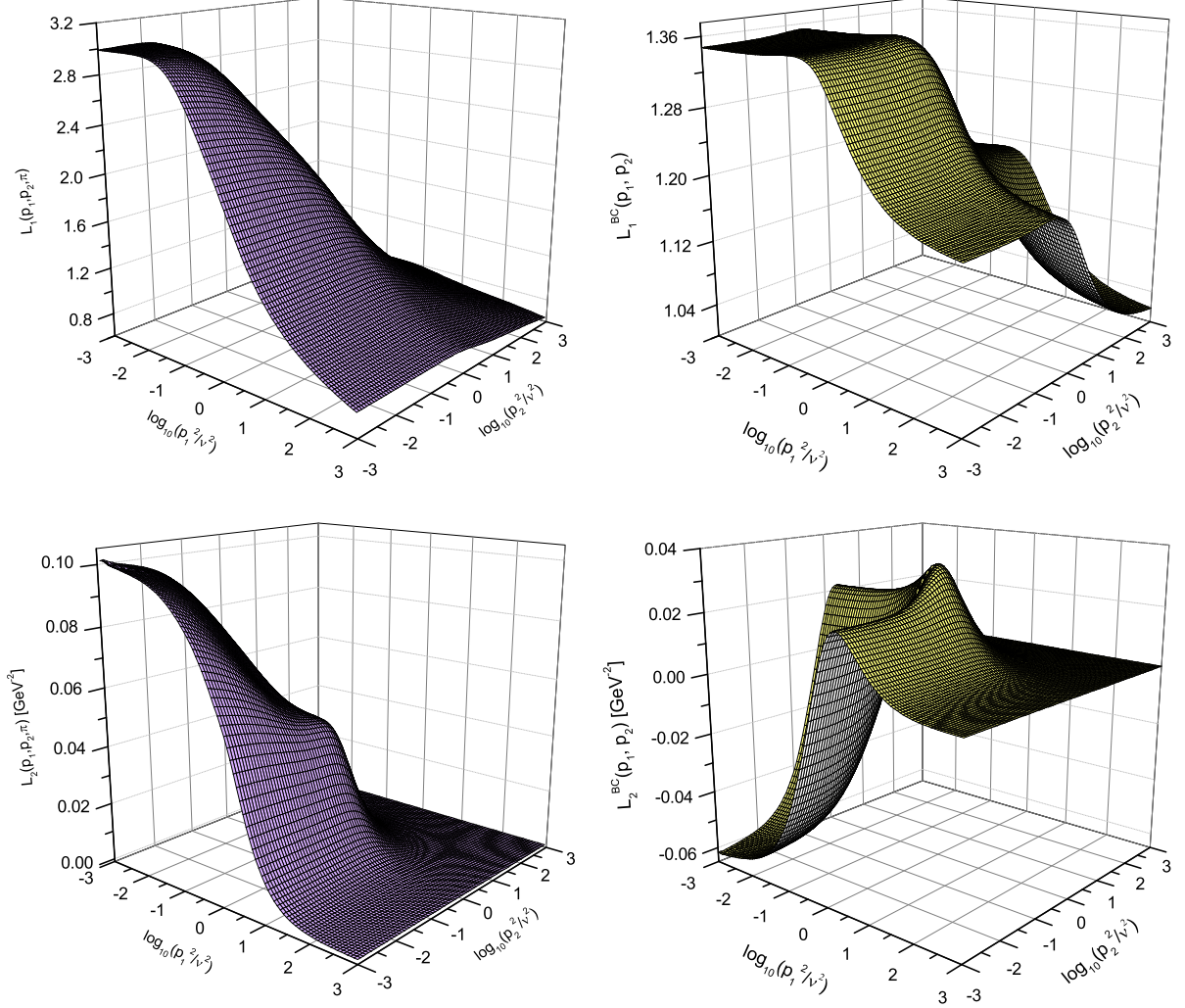


FIG. 14. The form factors  $L_1$  and  $L_2$  when  $\theta = \pi$  (left panels) and the corresponding  $L_1^{BC}$  and  $L_2^{BC}$  (right panels) for a higher value of the dynamical quark mass.

## V. SOME SPECIAL KINEMATIC LIMITS: 2-D PLOTS

In this section we concentrate on the determination of the form factors  $L_i$  in five different kinematic limits. The cases discussed will be the following:

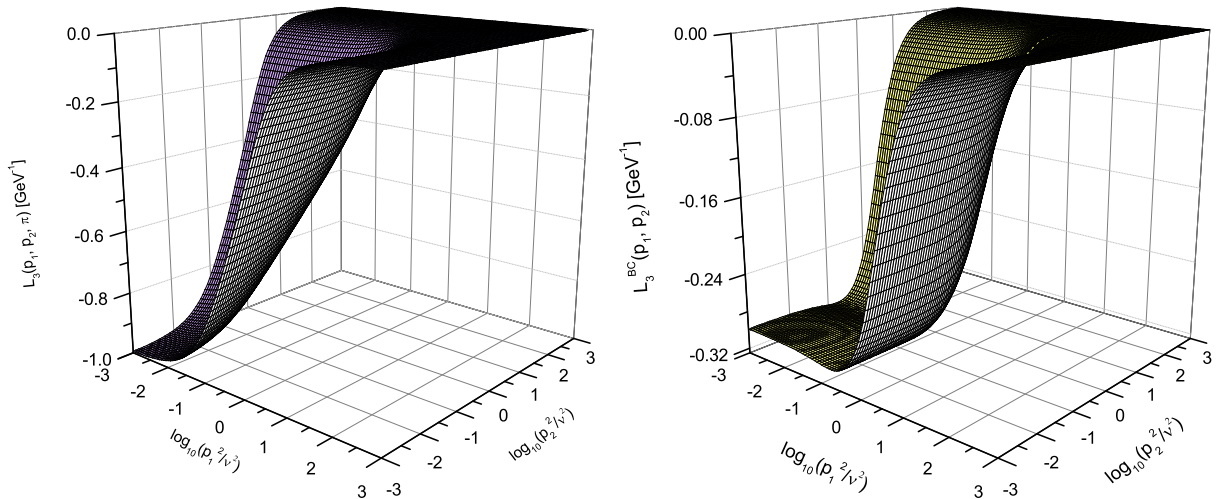


FIG. 15. The form factors  $L_3$  for  $\theta = \pi$  (left panel) and the corresponding  $L_3^{\text{BC}}$  (right panel) for a higher value of the dynamical quark mass.

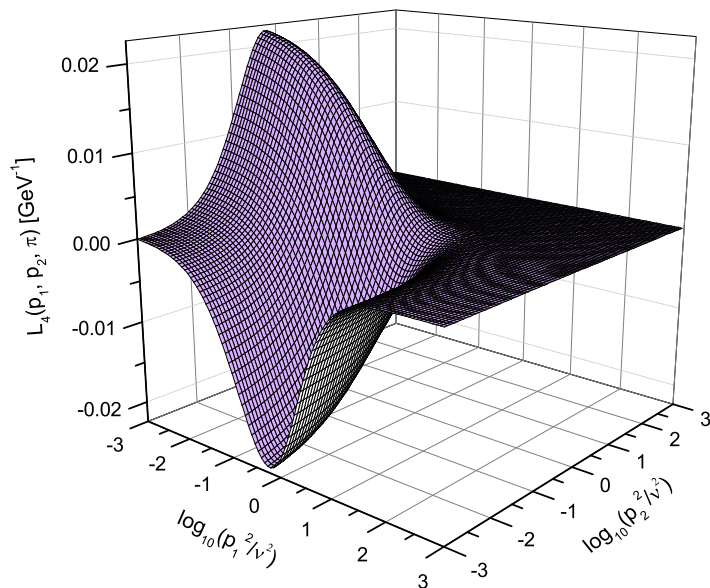


FIG. 16. The form factor  $L_4$  when  $\theta = \pi$  for a higher value of the dynamical quark mass.

(i) The soft gluon limit, which is defined when both momenta  $p_1$  and  $p_2$  have the same magnitude *i.e.*  $|p_1| = |p_2| = |p|$  and the angle between them is  $\theta = 0$ ;

(ii) The quark symmetric configuration, where again the two momenta have the same magnitude,  $|p_1| = |p_2| = |p|$ , but now they are anti-parallel *i.e.*,  $\theta = \pi$ ;

(iii) The soft anti-quark limit obtained when the anti-quark momentum vanishes, *i.e.*  $p_1 \rightarrow 0$  and  $p_2 \rightarrow p$ ;

(iv) The soft quark limit where  $p_2 \rightarrow 0$  and  $p_1 \rightarrow p$  ;

(v) The totally symmetric limit defined when the square of the three momenta of vertex are all equal, *i.e.*  $p_1^2 = p_2^2 = q^2 = p^2$  and the angle  $\theta = 2\pi/3$ .

Evidently, in all configurations listed above, the  $L_i$ s become functions of a single momentum variable, namely  $p$ . We will refer to the  $L_i$ s in each configuration as  $L_i^g(p)$ ,  $L_i^{sym}(p)$ ,  $L_i^{\bar{q}}(p)$ ,  $L_i^q(p)$  and  $L_i^{TS}(p)$ , respectively.

### A. Special kinematic limits

The determination of  $L_i$  in any of the above kinematic configurations may be performed in two different ways. The first is to consider the limit of interest directly at the level of Eq. (3.11), and then use the results obtained in Eq. (2.22). This particular procedure requires certain care, due to the presence of the function  $h$  in the various denominators. Specifically, in Euclidean space

$$h = p_1^2 p_2^2 \sin^2 \theta, \quad (5.1)$$

which vanishes when implementing the limits defining the cases (i)-(iv). Therefore, the numerators of the corresponding expressions in Eq. (3.11) must be appropriately expanded, and the potentially divergent terms explicitly canceled, by virtue of the exact vanishing of certain angular integrals. A detailed description of this procedure for the cases (i) and (ii) will be outlined in the Appendix A. The second way is to exploit directly the numerical results obtained for general configurations, since all special kinematic limits constitute particular projections (“slices”) of the 3-D results. Evidently, the results obtained with both methods ought to coincide.

For example, the plane defined by the equation  $p_1 = p_2$  in the left panel of Fig. 8 corresponds to the slice that defines  $L_1^g(p)$ , since the angle in this figure is fixed at  $\theta = 0$ . This particular slice was isolated in the top left panel of Fig. 17 and it is represented by the black continuous line.

As we can see,  $L_1^g(p)$  displays a smooth behavior, decreasing monotonically towards the ultraviolet region. It is important to stress that the fact that  $L_1^g(\mu) \neq 1$  is not in contradiction with the renormalization condition employed in the calculation [see Eq. (4.2)], which ensures that the  $L_1$  will be equal to the unity in the totally symmetric point, defined when  $p_1^2 = p_2^2 = q^2 = \mu^2$ .

Now, following the same procedure outlined before, we can extract the other non-vanishing form factors, namely  $L_2^g(p)$  and  $L_3^g(p)$ . For the purpose of comparison, we also plot in the top left panel of Fig. 17 the dimensionless combinations  $p^2L_2^g(p)$  (red dashed line) and  $-pL_3^g(p)$  (blue dash-dotted line). We clearly see that both vanish in the infrared limit, and they are evidently much more suppressed than  $L_1^g(p)$ .

Next, we turn to the quark symmetric configuration. In the top right panel of the Fig. 17, we show the various  $L_i^{sym}(p)$ . In particular, the projection of  $L_1^{sym}(p)$  (black continuous line) corresponds to the slice defined by the plane  $p_1 = p_2$  of the right panel of Fig. 12 ( $\theta = \pi$ ). Even though the tensorial structures  $\lambda_2^\mu$ ,  $\lambda_3^\mu$  and  $\lambda_4^\mu$  defined in Eq. (2.12) vanish in the quark symmetric limit, the form factors  $L_2^{sym}(p)$  and  $L_3^{sym}(p)$  are nonvanishing. For this reason, we show in the same plot  $p^2L_2^{sym}(p)$  (red dashed) and  $-pL_3^{sym}(p)$  (blue dash-dotted); again, both quantities are rather suppressed when compared to  $L_1^{sym}(p)$ .

The next quantities of interest are the  $L_i^{\bar{q}}(p)$ , shown in the bottom left panel of Fig. 17. Note that, as can be easily confirmed by means of an analytic derivation,  $L_i^{\bar{q}}(p)$  is independent of the angle  $\theta$ . For this reason, when we select the plane where  $p_1 = 0$  (for practical purposes  $p_1 \approx 30$  MeV), in any of the plots shown in the Figs. 7, 9, 10 and 11, we obtain the same result for all  $L_i^{\bar{q}}(p)$ , respectively.

Turning to  $L_i^q(p)$ , note that when we combine Eq. (2.8) with Eqs. (2.11) and (2.22), one concludes that  $L_i^{\bar{q}}(p) = L_i^q(p)$  with  $i = 1, 2, 3$ , while  $L_4^{\bar{q}}(p) = -L_4^q(p)$ ; this happens because the first three tensorial structures in Eq. (2.11) are symmetric under  $p_1 \leftrightarrow p_2$ , while the fourth is antisymmetric. Therefore, the numerical results for  $L_1^q(p)$ ,  $p^2L_2^q(p)$  and  $-pL_3^q(p)$  coincide with those shown in the bottom left panel of the Fig. 17, except for  $pL_4^q(p)$  (green dotted line), which reverses its sign.

Finally,  $L_i^{TS}(p)$  is obtained by selecting the plane where  $p_1^2 = p_2^2$  in the 3-D plots where  $\theta = 2\pi/3$ , such as the one for  $L_1$  shown on the left panel of Fig. 12. The results of these projections are shown in the bottom right panel of Fig. 17.

It is interesting to notice that all  $L_i$  display a very similar pattern. More specifically, all  $L_1$  have narrow peaks of similar size located in the region of a few MeV, and then decrease logarithmically in the ultraviolet, whereas  $p^2L_2$  and  $-pL_3$  are rather suppressed quantities, vanishing in both the infrared and ultraviolet limits.

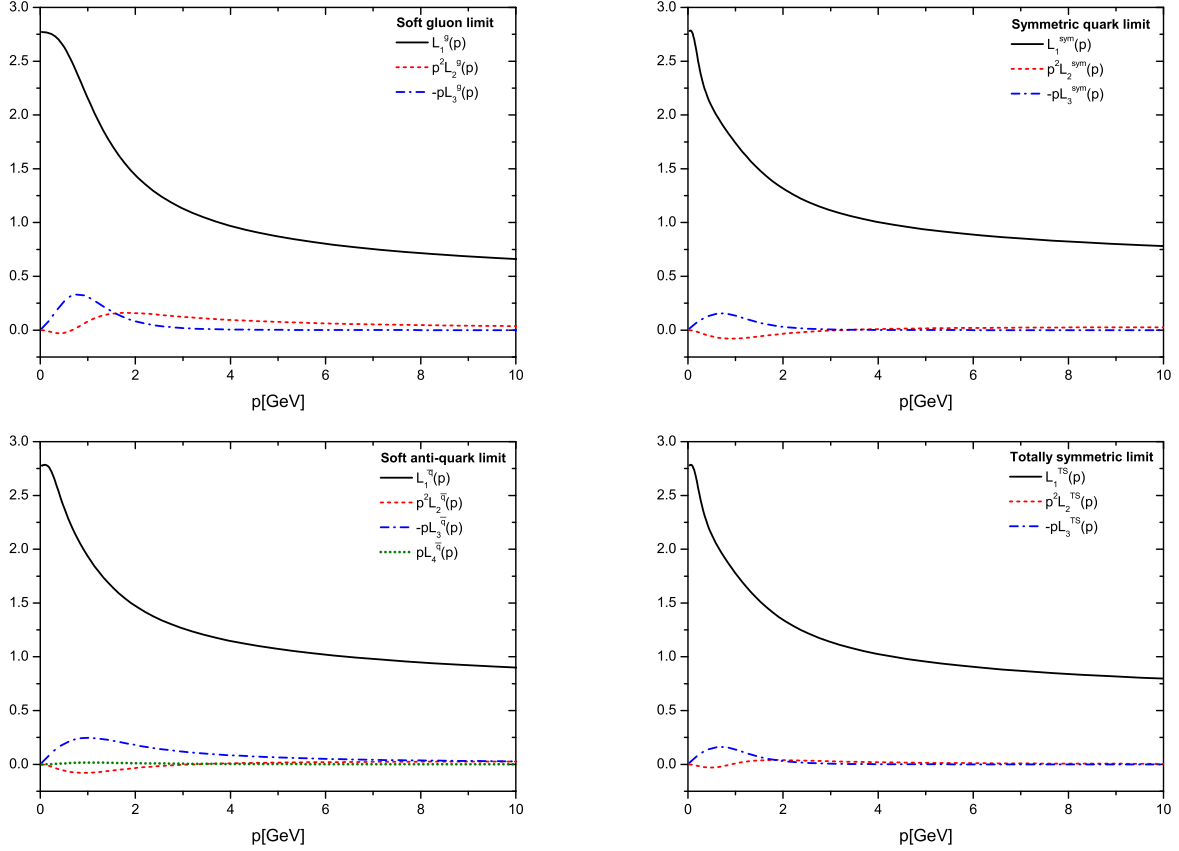


FIG. 17. The form factors  $L_i$ s for different kinematic configurations. The  $L_i^g$  (top left panel) are the form factors in the soft gluon configuration. The  $L_i^{sym}$  (top right panel) represents the quark symmetric case. The  $L_i^{\bar{q}}$  (or  $L_i^q$ ) (bottom left panel) is in the soft anti-quark (or quark) limit, whereas  $L_i^{TS}$  (bottom right panel) is the totally symmetric configuration.

## B. A closer look at the soft gluon limit

We will next consider the one-loop result for  $L_1^g(p)$ , which will furnish some additional insights on the asymptotic (ultraviolet) behavior of this form factor, shown in the top left panel of Fig. 17. The derivation of the one-loop expression for  $L_1^g(p)$  may proceed in two different ways: the first is based on the direct calculation of the one-loop diagrams shown in Fig. 18, for this particular kinematics; the second consists of substituting one-loop results for the ingredients entering in the all-order relation captured by Eq. (2.22). Evidently, the answers obtained with either method ought to coincide.

Following [44], we employ dimensional regularization for the direct one loop calculation;

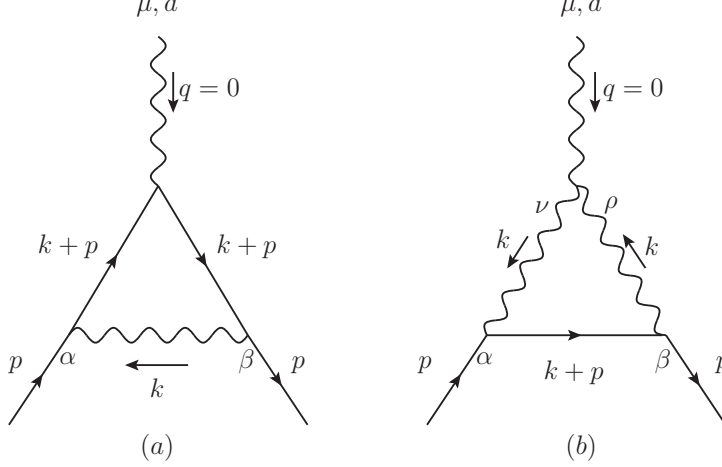


FIG. 18. The one-loop diagrams of the quark-gluon vertex in the soft gluon limit.

specifically, the measure of Eq. (3.2) becomes

$$\int_l \rightarrow \frac{\mu^\epsilon}{(2\pi)^d} \int d^d l, \quad (5.2)$$

where  $d = 4 - \epsilon$  and  $\mu$  is the 't Hooft mass scale.

It is then relatively straightforward to demonstrate that in the Landau gauge the “abelian” diagram (a) vanishes exactly in the soft gluon limit (before renormalization) [44]; note that the derivation of this result requires the use of dimensional regularization formulas such as  $\gamma_\mu \gamma_\nu \gamma^\mu = (2 - d)\gamma_\nu$  for the corresponding “Diracology”, instead of the usual  $\gamma_\mu \gamma_\nu \gamma^\mu = -2\gamma_\nu$ . The evaluation of diagram (b) yields (in Euclidean space)

$$L_{1\text{pert}}^g(p) = 1 + \frac{C_A \alpha_s}{16\pi} \left[ -3 \ln \left( \frac{p^2 + m_0^2}{\mu^2 + m_0^2} \right) + \frac{m_0^4}{p^4} \ln \left( \frac{p^2 + m_0^2}{m_0^2} \right) - \frac{m_0^4}{\mu^4} \ln \left( \frac{\mu^2 + m_0^2}{m_0^2} \right) - m_0^2 \left( \frac{1}{p^2} - \frac{1}{\mu^2} \right) \right], \quad (5.3)$$

where  $m_0$  is the current quark mass, which guarantees the infrared finiteness of the result. In addition, note that the above expression was renormalized using the MOM scheme, imposing the condition  $L_{1\text{pert}}^g(\mu^2) = 1$ . Turning to the second way, the substitution of  $p_1 = p_2 = p$  ( $q = 0$ ) into Eq. (2.22), and the use of the fact that  $X_i = \bar{X}_i$ ,  $X_0 = 1$  and  $X_1 = -X_2$  in this limit, yields (in Euclidean space)

$$L_1^g(p) = F(0) [A(p)(1 + 2p^2 X_3(p)) - 2B(p)X_1(p)]. \quad (5.4)$$

The determination of  $L_{1\text{pert}}^g(p)$  from Eq. (5.4) is rather subtle, and involves the exact cancellation of two infrared divergent contributions stemming from two of the ingredients

appearing in it. We start by recalling that  $F$  at one-loop level is given by

$$F^{\text{pert}}(q^2) = 1 - \frac{3C_A\alpha_s}{16\pi} \ln\left(\frac{q^2}{\mu^2}\right), \quad (5.5)$$

which clearly displays an infrared divergence of the type “ $\ln 0$ ” when  $q^2 \rightarrow 0$ , due to the presence of the “unprotected” logarithm; of course, nonperturbatively the infrared divergence of this logarithm is known to be tamed, and a finite value for  $F(0)$  is obtained (see, e.g., [49]). Since  $L_{1\text{pert}}^g(p)$  displays no such divergence, an exact cancellation against a similar contribution must take place. To establish the precise mechanism that makes this happen, we set in Eq. (A4)  $p_1 = p_2 = p$ ,  $\theta = 0$ , and the tree-level expressions  $A(p) = 1$ ,  $B(p) = m_0$ ,  $F(q) = 1$  and  $\Delta(q) = 1/q^2$ , and after restoring the measure we obtain

$$\begin{aligned} X_1^{\text{pert}}(p) &= i\frac{C_A g^2}{6} \int_k \left[ 2 + \frac{(k \cdot p)^2}{k^2 p^2} \right] \frac{m_0}{k^4[(k+p)^2 - m_0^2]}, \\ p^2 X_3^{\text{pert}}(p) &= -i\frac{C_A g^2}{6} \int_k \left[ 2p^2 + 3(k \cdot p) + \frac{(k \cdot p)^2}{k^2} \right] \frac{1}{k^4[(k+p)^2 - m_0^2]}. \end{aligned} \quad (5.6)$$

A systematic inspection of the above terms reveals that the only source of such a divergent contribution is the third term in  $p^2 X_3^{\text{pert}}(p)$ . Focusing on this term and applying Feynman parametrization, one may eventually identify a contribution of the form  $\frac{3C_A\alpha_s}{16\pi} \int_0^1 dx/x$ , which allows for the necessary cancellation to go through. As it should, the final result coincides with that of Eq. (5.4).

In Fig. 19 we compare our nonperturbative result for  $L_1^g(p)$  (black continuous line) with the one-loop expression of Eq. (5.4) (red dashed line). Notice that, in order to perform a meaningful comparison, we renormalize both curves imposing the same renormalization condition, *i.e.*,  $L_1^g(\mu) = L_{1\text{pert}}^g(\mu) = 1$ . Clearly, we see a qualitative agreement between both curves for large values of  $p$ . Evidently, the small deviations between these curves in the ultraviolet is expected, and can be attributed to the higher order loop corrections that  $L_1^g(p)$  contains in it.

We also show in the Fig. 19  $L_1^g(p)$  renormalized in the totally symmetric configuration (blue dash-dotted line), which satisfies the renormalization condition imposed by Eq. (4.2). This curve is the same one (black continuous) shown in the top left panel of Fig. 17. Therefore, the small quantitative difference between the black continuous and the blue dash-dotted curves shown in the Fig. 19 is merely the effect of the imposition of different renormalization conditions.

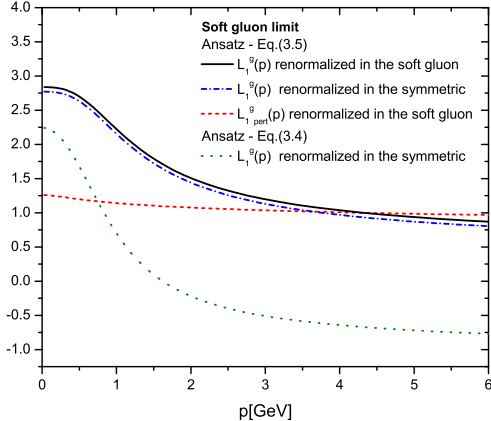


FIG. 19. Comparison of the one-loop result  $L_{1\text{pert}}^g(p)$  (red dashed), given in Eq. (5.4) with  $L_1^g(p)$  obtained with the Ansatz given by Eq. (3.5) and renormalized in the two different configurations: (i) soft gluon configuration, *i.e.*  $L_1^g(\mu) = 1$  (black continuous) and (ii) totally symmetric configuration given by Eq. (4.2) (blue dash-dotted line). In addition, we show the  $L_1^g(p)$  renormalized in the totally symmetric configuration obtained with the Ansatz given by Eq. (3.4) (green dotted line).

In order to expose how the Ansatz of Eq. (3.4) affects dramatically the perturbative behavior of the soft gluon configuration, in Fig. 19 we show the result for  $L_1^g(p)$  computed with Eq. (3.4) (green dotted line). Notice that this curve corresponds to the “slit” (slice where  $p_1 = p_2$ ) shown in the right panel of Fig. 8. Since the result in Fig. 8 is renormalized in the totally symmetric configuration, the (green) dotted curve should be compared with the (blue) dash-dotted line, which was obtained employing the Ansatz of the Eq. (3.5). The sizable deviation of the green dotted line from the expected perturbative region, where all the others curves are located, clearly indicates that the Ansatz of Eq. (3.4) is not an appropriate choice. Evidently, the use of Eq. (3.4) provides excessive strength in the single component of the vertex considered; in fact, as we notice in Fig. 13, the combination  $F(q)L_1^{\text{BC}}(p_1, p_2)$  is indeed more enhanced than the solution for the complete  $L_1(p_1, p_2, \theta)$ .

For completeness, in Fig. 20, we show the contribution of each of the individual terms appearing in the Eq. (5.4). We start showing the contribution of the first term which corresponds to the “minimal” non-Abelian BC vertex (purple dashed curve),  $F(0)A(p)$ . In the plot, we clearly see that when we neglect all the  $X_i$  contributions,  $L_1^g(p) \rightarrow F(0)$  when  $p \rightarrow \infty$ . Now, let us turn on the contribution of the  $X_1$  (green dotted line); given that  $X_1$  is multiplied by  $B(p)$ , it is clear that it can only modify the infrared and intermediate regions of  $L_1^g(p)$ , leaving the ultraviolet behavior intact. Focusing on the most interesting

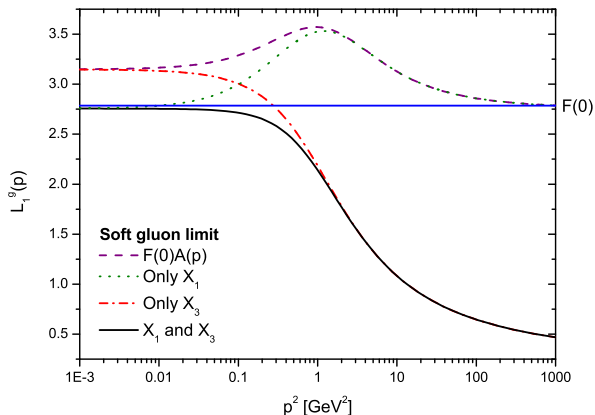


FIG. 20. The individual contributions entering into the definition of  $L_1^g(p)$ , given in Eq. (5.4).

term, namely  $X_3$ , we first note that, since it is multiplied by  $p^2$ , it does not change the infrared limit (red long-dashed dotted line). However, since  $X_3$  is negative and quite sizable (see bottom right panel of Fig. 6), it has a considerable influence on the intermediate and ultraviolet regions of  $L_1^g(p)$ , producing a notable decrease in its behavior, as shown by the case where all contributions of Eq. (5.4) are taken into account (black continuous curve).

As an additional remark in this subsection, we emphasize that the numerical calculation of the full  $X_3$  when  $\theta \approx 0$  and  $p_1^2 \approx p_2^2$  expressed by Eq. (A4) is rather delicate. More specifically, when one fixes the values of the external momenta  $p_1^2$  and  $p_2^2$  at infrared or intermediate scales (order of  $10^{-3} - 1 \text{ GeV}^2$ ), the resulting integrand of Eq. (A4) is relatively smooth. However, as one increases the momenta towards the ultraviolet region, the integrand develops sharp peaks, whose width decreases as the momenta increase or/and as  $p_1$  gets close to  $p_2$ . A precise numerical treatment of these peaks requires a refined grid, especially because minor errors in the integration may be subsequently amplified due to the multiplication by  $p^2$ , as happens in the case of  $L_1^g(p)$  given by Eq. (5.4). In fact, an earlier analysis [67] using a less sophisticated numerical treatment of these peaks gave rise to an artificial increase of  $L_1^g(p)$  in the ultraviolet region. Interestingly enough, the recent lattice simulations for  $L_1^g(p)$  of Ref. [42, 43] found a similar increase around the same region, which the authors seem to attribute to lattice artifacts.

We end this section by suggesting to the reader that, in view of the above observations, the results presented in this work for the soft-gluon limit ought to be considered as provisional. Indeed, even though an appropriate choice of the quark-gluon Ansatz used in evaluating  $H$ ,

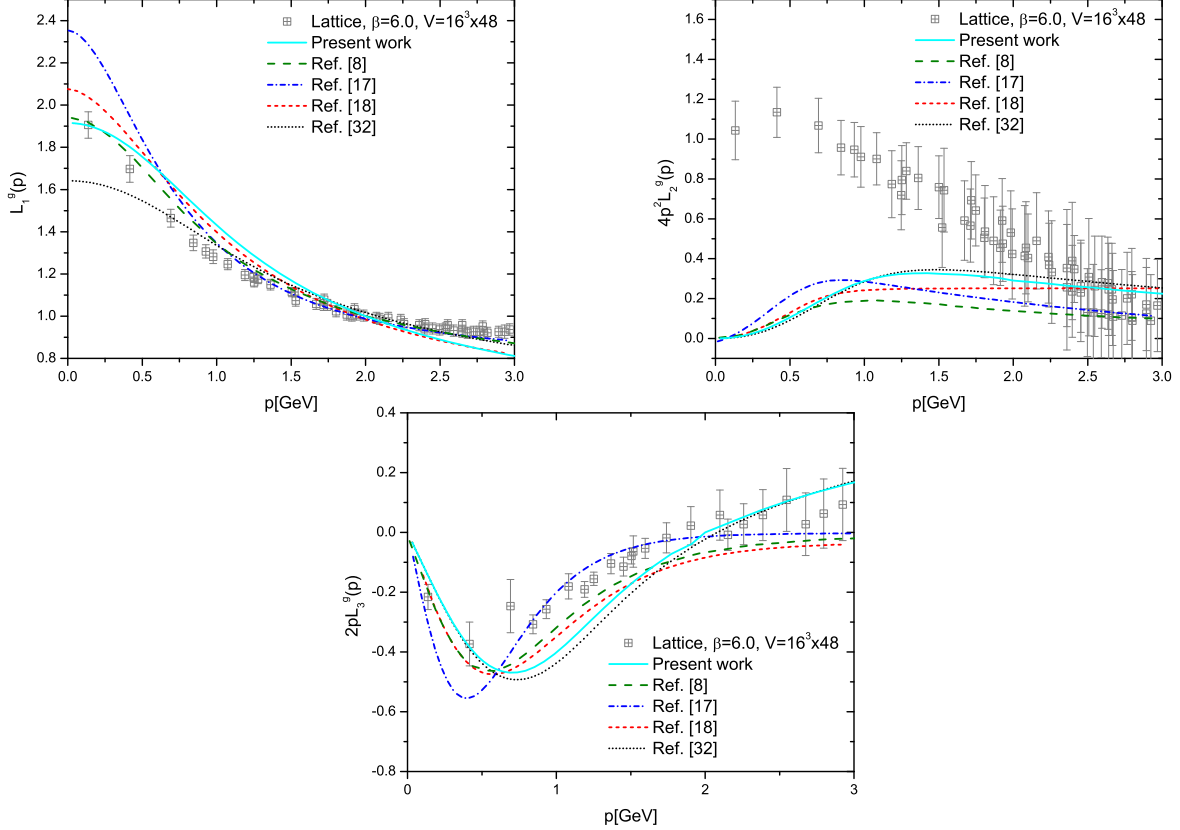


FIG. 21. Comparison of our results (cyan continuous line) in the soft gluon configuration with the previous analytical results obtained in the Refs. [8] (green dashed), [17] (blue dashed dot), [18] (red short dashed) and [32] (black dotted), and the available lattice data (squares) of Ref. [38, 39].

*i.e.*, the transition from Eq.(3.4) to Eq.(3.5), appears to alleviate considerably the problem of the unnatural ultraviolet suppression, and despite a vast array of checks implemented on our integration routines, the possibility that an unresolved numerical issue may still be lurking has not been conclusively discarded.

## VI. COMPARISON WITH PREVIOUS WORKS

In this section we compare our results for the quark-gluon vertex in the soft gluon configuration with those obtained in a variety of earlier works appearing in the literature. The reason for choosing this particular configuration is because it is the most widely explored in the literature, and because is one of the few that can be individually isolated in lattice simulations without being “contaminated” by transverse contributions.

Here we will concentrate on the results presented in the Refs [8, 17, 18, 32]. Let us start by

recalling that in Refs. [17, 18] an approximate version of the SDE governing the quark-gluon vertex was considered, retaining the one-loop dressed diagrams that compose the skeleton expansion of  $\Gamma_\mu$ . The main difference between the works of Ref. [17] and Ref. [18] originates from the functional form employed for the gluon propagator,  $\Delta(q^2)$ . In the case of Ref. [17], the “rainbow-ladder” approximation was used, and the product  $g^2\Delta(q^2)$  was replaced by a phenomenologically motivated *Ansatz* [6]. Instead, in Ref. [18], the one-loop dressed diagrams were computed using as nonperturbative ingredients the quark and gluon propagators calculated within the “ghost dominance” formalism [3, 23]. In Ref. [8], the authors instead of using the Schwinger-Dyson approach, they construct the three-particle irreducible (3PI) effective action to three loops to determine the quark-gluon vertex structure. To do that, they use as input the gluon and the ghost propagators which are in agreement with lattice results of Ref. [68]. Finally, in Ref. [32] an improved version of the gauge technique was employed, where the transverse form factors were estimated by resorting to the so-called transverse Ward identities [53–58], and the nonperturbative ingredients such as  $\Delta(q^2)$  and  $F(q^2)$  were taken from the lattice [49]. Of particular interest for the present work are the numerical results for the soft gluon configuration reported in [32].

In order to make a direct contact with the lattice data of Refs. [36, 38], it is important to mention that their results were obtained using a current quark mass of  $m_0 = 115$  MeV. Moreover, the relevant form factors were renormalized at the scale  $\mu' = 2$  GeV. Therefore, for the sake of comparison, we will also employ, exclusively in this section, a new set of inputs for  $A(p)$ ,  $B(p)$ ,  $\Delta(q)$ ,  $F(q)$  with the aforementioned characteristics. To obtain these new inputs, we follow the same procedure outlined in the Ref. [32], fixing  $\alpha(\mu') = 0.45$ , which permits a better agreement with the lattice data.

In Fig. 21 we compare our results for the soft gluon form factors  $L_1^g$ ,  $4p^2L_2^g(p)$  and  $2pL_3^g(p)$  (cyan curves) with those obtained in the analysis presented in Refs. [8] (green dashed), [17] (blue dashed-dot) and [18] (red short dashed). In addition, on the same plot, we show the results of Ref. [32] (black dotted), and the lattice data obtained in Ref. [38, 39] (squares). In the case of the form factors  $L_1^g$  and  $2pL_3^g$ , our results show rather good agreement with both the lattice simulations and the previous analytical studies. In the case of  $4p^2L_2^g$  [top right panel of Fig. 21], our result agrees with the general pattern found by all previous analytic determinations; in particular, all curves share the characteristic feature of vanishing at the origin. However, as may be plainly established from Fig. 21, our result, and all others, are

vastly different from the curve found on the lattice.

## VII. RGI INTERACTION KERNELS

As a direct application of some of the results obtained in the previous sections, we turn to the construction of RGI ( $\mu$ -independent) combinations that, depending on the truncation schemes employed, quantify the strength of a *particular piece* of the effective (momentum-dependent) interaction between quarks. Specifically, we will consider the dressed “one-gluon exchange” approximation of the kernel appearing in a typical Bethe-Salpeter equation [panel (a) of Fig. 22], and the corresponding kernel entering in the gap equation that determines the dynamically generated constituent quark mass [panel (b) of Fig. 22].

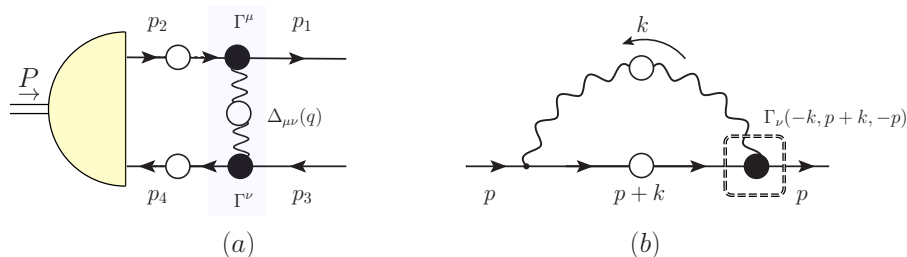


FIG. 22. Panel (a): The one-loop dressed gluon exchange that typically appears in the Bethe-Salpeter equation. Panel (b): The complete quark self-energy entering in the definition of the gap equation.

### A. Underlying assumptions

The main objective of this section is to consider the part of the interaction kernel that is of the form  $L_1 \gamma_\mu P^{\mu\nu}(q) \gamma_\nu L_1$ , neglecting all other tensorial structures. Motivated by the discussion presented in section III regarding the way that the choice of the basis for  $\Gamma_\mu^{(\text{ST})}$  may affect amplitudes containing the combination  $\Gamma_\mu^{(\text{ST})} P^{\mu\nu}(q) \Gamma_\nu^{(\text{ST})}$ , it is important to emphasize at this point some of underlying assumptions of the ensuing analysis.

1. As has been explained following Eq.(2.21), if one considers the combination  $P^{\mu\nu}(q) \Gamma_\nu^{(\text{ST})}$ , with no reference to the transverse parts, the result depends crucially on the choice of the basis for  $\Gamma_\mu^{(\text{ST})}$ . In particular, as has been exemplified with the case of  $L_1$ , the

transversely projected  $\Gamma_\nu^{(\text{ST})}$  may acquire any value whatsoever, through appropriate choice of the basis elements.

2. The class of bases that we consider contain the classical tensor  $\gamma_\mu$  as a genuine element of the tensors that span  $\Gamma_\mu^{(\text{ST})}$ , *without* any admixture of transverse components. Put in the language of section III, in Eq.(2.18) we have  $c = 0$ , or, equivalently, in Eq.(2.19) we have  $\Gamma_\mu^{[0]} = \lambda_{1,\mu}$ . Evidently, the BC basis employed throughout our analysis is precisely of this particular type.
3. One may rephrase the previous point in the following way. Let us imagine for a moment that all quantum corrections are switched off; then, unambiguously,  $\Gamma_\mu P^{\mu\nu}(q)\Gamma_\nu \rightarrow \Gamma_\mu^{[0]} P^{\mu\nu}(q)\Gamma_\nu^{[0]} = d - 1$ . Therefore, one may fix the amount of  $L_1$  by requiring that, when one sets  $L_1 = 1$ , the above result is reproduced (that forces  $c = 0$ ).
4. Of course, the above “normalization” does not fix the values of the “ $c_i$ ” that control the amount of  $L_2$ ,  $L_3$  and  $L_4$  entering in the answer. In what follows we will simply set  $L_2 = L_3 = L_4 = 0$  by hand, even though the basis used (BC) does *not* furnish  $c_i = 0$  for them.

## B. Bethe-Salpeter kernel

As mentioned above, one can see in the panel (a) of Fig. 22, that the kernel of the Bethe-Salpeter equation receives contributions not only from the full gluon propagator but also from the fully-dressed quark-gluon vertices. To simplify the analysis, let us consider only the part of  $\Gamma_\mu$  that is proportional to  $\gamma_\mu$ , *i.e.*,  $\Gamma_\mu = L_1\gamma_\mu$ . Then, the strength of this effective interaction may be described by means of a scalar quantity, to be denoted by  $\mathcal{Q}(q, -p_1, p_3)$ , given by

$$\mathcal{Q}(q, -p_1, p_3) = \alpha_s \Delta(q) \left[ \frac{L_1(q, p_2, -p_1) L_1(-q, p_3, -p_4)}{A(p_2) A(p_4)} \right]. \quad (7.1)$$

This particular quantity is  $\mu$ -independent, as one may verify by employing the standard renormalization relations

$$\begin{aligned}
S_R(p; \mu) &= Z_F^{-1}(\mu)S(p), \\
\Delta_R(q; \mu) &= Z_A^{-1}(\mu)\Delta(q), \\
\Gamma_R^\nu(p, k, q; \mu) &= Z_1(\mu)\Gamma^\nu(p, k, q), \\
g_R(\mu) &= Z_g^{-1}(\mu)g = Z_1 Z_F^{-1} Z_A^{-1/2} g,
\end{aligned}
\tag{7.2}$$

where  $Z_F$ ,  $Z_A$ ,  $Z_1$ , and  $Z_g$  are the corresponding renormalization constants<sup>6</sup>.

It is interesting to compare  $\mathcal{Q}$  to a closely related quantity, defined in the recent literature [70]. In particular, a field-theoretic construction based on the pinch technique allows the definition of a process- and  $\mu$ -independent combination, denoted by

$$\widehat{d}(q^2) = \frac{\alpha_s(\mu)\Delta(q^2)}{[1 + G(q^2)]^2},
\tag{7.3}$$

where  $G(q^2)$  is the transverse component of a special Green's function [71, 72], akin to a ghost-gluon “vacuum polarization”, which arises in contemporary applications of the aforementioned technique [66, 70, 73, 74]. From  $\widehat{d}(q^2)$  one may define the dimensionless quantity

$$\mathcal{I}_{\widehat{d}}(q^2) = q^2 \widehat{d}(q^2),
\tag{7.4}$$

which, as explained in detail in [70], makes direct contact with the interaction strength obtained from a systematic “bottom-up” treatment, where bound-state data are fitted within a well-defined truncation scheme [75].

Given that  $\widehat{d}(q^2)$  is a function of a single kinematic variable, a meaningful comparison with  $\mathcal{Q}(q, -p_1, p_3)$  may be accomplished by computing the latter in a special kinematic limit. Specifically, we choose to evaluate both  $L_1(q, p_2, -p_1)$  and  $L_1(-q, p_3, -p_4)$  at their corresponding totally symmetric points, namely  $p_1^2 = p_2^2 = q^2$  and  $p_3^2 = p_4^2 = q^2$ , thus converting  $\mathcal{Q}$  to a function of the single variable,

$$\mathcal{Q}(q^2) = \alpha_s(\mu)\Delta(q^2) \left[ \frac{L_1^{\text{TS}}(q^2)}{A(q^2)} \right]^2,
\tag{7.5}$$

---

<sup>6</sup> In the Landau gauge,  $Z_F = 1$  at *one loop*, and, therefore, one may omit the factor  $A^{-1}(p_2)A^{-1}(p_4)$  in the definition of  $\mathcal{Q}(q, -p_1, p_3)$ , which would then be  $\mu$ -independent at that order. Note, however, that higher loops make  $Z_F$  non-trivial [69], and thus, the inclusion of this factor becomes necessary.

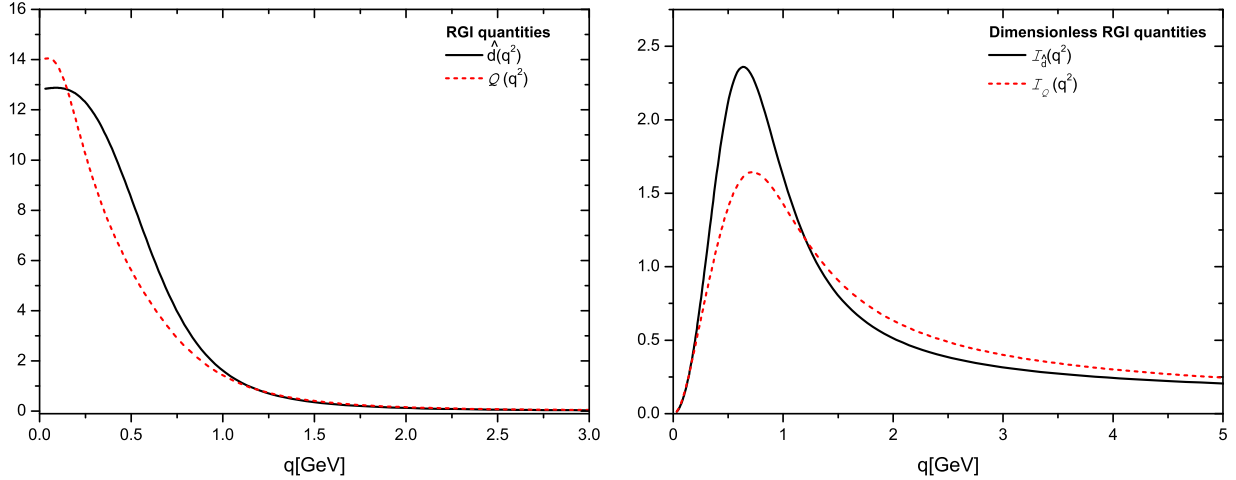


FIG. 23. Comparison of the dimensionful RGI quantities  $\hat{d}(q^2)$  and  $\mathcal{Q}(q^2)$  defined in the Eqs. (7.3) and (7.5), respectively (left panel) and their dimensionless counterparts  $\mathcal{I}_{\hat{d}}(q^2)$  and  $\mathcal{I}_{\mathcal{Q}}(q^2)$  given by Eqs. (7.4) and (7.6) (right panel).

where the behavior of  $L_1^{\text{TS}}(q)$  is given by the bottom right panel of Fig. 17. Evidently, the dimensionless quantity analogous to  $\mathcal{I}_{\hat{d}}(q^2)$  is given by

$$\mathcal{I}_{\mathcal{Q}}(q^2) = q^2 \mathcal{Q}(q^2). \quad (7.6)$$

Note that, for asymptotically large  $q^2$ , both  $\mathcal{I}_{\hat{d}}(q^2)$  and  $\mathcal{I}_{\mathcal{Q}}(q^2)$  capture the one-loop running coupling of QCD [66].

On the left panel of Fig. 23 we compare  $\mathcal{Q}(q^2)$  and  $\hat{d}(q^2)$ . For obtaining  $\hat{d}(q^2)$  (black continuous line), we use the same value for  $\alpha_s(\mu)$  as in [70], namely  $\alpha_s(\mu) = 0.22$  for  $\mu = 4.3$  GeV; the determination of this value entails a subtle combination of 4-loop perturbative results, nonperturbative information included in the vacuum condensate of dimension two, and the extraction of  $\Lambda_{\text{QCD}}$  from lattice results of the ghost-gluon vertex in the Taylor kinematics [76]. Instead, for computing  $\mathcal{Q}(q^2)$  (red dashed line) self-consistency dictates that one must set in Eq. (7.5)  $\alpha_s(\mu) = 0.28$ , because this is precisely the value used for obtaining  $A(q^2)$  and  $L_1^{\text{TS}}(q^2)$  in Sections IV A and V, respectively.

On the right panel of the same figure, we show  $\mathcal{I}_{\mathcal{Q}}(q^2)$  and  $\mathcal{I}_{\hat{d}}(q^2)$ . We clearly see that,  $\mathcal{I}_{\hat{d}}(q^2)$  displays a higher peak in the region of about 650 MeV, while  $\mathcal{I}_{\mathcal{Q}}(q^2)$  has its peak around 730 MeV. Notice that  $\mathcal{I}_{\mathcal{Q}}(q^2)$  is consistently higher in the interval between 1.25 – 5 GeV.

In order to obtain an indication of the *integrated strength* furnished by these curves,

following [70] we may introduce the integral

$$W_{\mathcal{I}} = \int_0^{q_0^2} dq^2 \mathcal{I}(q^2), \quad (7.7)$$

where  $q_0 \approx 5$  GeV is the value of the momentum where the two  $\mathcal{I}(q)$  practically merge into each other in Fig. 23. The results of the integration are  $W_{\mathcal{I}} = 10.4$  GeV<sup>2</sup> when  $\mathcal{I} = \mathcal{I}_{\hat{d}}$  and  $W_{\mathcal{I}} = 11.3$  GeV<sup>2</sup> when  $\mathcal{I} = \mathcal{I}_{\mathcal{Q}}$ .

Interestingly, while  $\mathcal{Q}(q^2)$  appears quite suppressed relative to  $\hat{d}(q^2)$  in the range of momenta between 0.15 – 1.1 GeV, the corresponding integrated strengths turn out to be rather close to each other; in fact,  $\mathcal{Q}(q^2)$  is 8.6% larger than  $\hat{d}(q^2)$ .

Even though the amount of physical information contained in  $\mathcal{Q}(q^2)$  and  $\hat{d}(q^2)$  is a-priori different, given that the two quantities originate from distinct truncation schemes, the simple analysis presented above seems to suggest a certain similarity in the structures obtained using either of them. One should keep in mind, of course, that all remaining tensorial structures of the quark-gluon vertex (transverse and non-transverse), which are certainly non-negligible, must be properly taken into account (within both frameworks), before any robust conclusion on this matter may be drawn.

### C. Gap equation kernel

We end with a preliminary look at the kernel that enters in the standard quark gap equation formulated in the Landau gauge. In particular, the fully-dressed quark-gluon vertex  $\Gamma_\mu$  constitutes a central ingredient of the quark self-energy, shown in the panel (b) of Fig. 22; evidently,  $(q, p_2, -p_1) \rightarrow (p - k, k, -p)$ , and, eventually, in order to treat the full question of chiral symmetry breaking, two out of the three momenta of this particular vertex are to be integrated over, since the virtual momentum  $k$  circulating in the loop enters in them.

For the purposes of this introductory discussion, we consider a “frozen” kinematic configuration, *i.e.*, no integration over  $k$  will be implemented, and simplify the analysis by using the approximation  $\Gamma_\mu = L_1 \gamma_\mu$ . Then, the gap equation assumes the form

$$S^{-1}(p) = \not{p} - 4\pi C_F \int_k \gamma_\mu \frac{1}{(\not{p} + \not{k}) - \mathcal{M}(p+k)} \gamma_\nu P^{\mu\nu}(k) K_{\text{gap}}(-k, k+p, -p), \quad (7.8)$$

where  $C_F = 4/3$  is the Casimir eigenvalue in the fundamental representation, and

$$K_{\text{gap}}(-k, k+p, -p) = \alpha_s(\mu) \Delta(k^2) F(k^2) \left[ \frac{L_1(-k, k+p, -p)}{A(p+k)} \right]. \quad (7.9)$$

As has been discussed in detail in [4], the appearance of the factor  $F(k^2)$  in  $K_{\text{gap}}$  accounts in an effective way for contributions originating from the transverse part of the quark-gluon vertex, which, if properly treated, would combine with the renormalization constant  $Z_1$  that multiplies the quark self-energy, furnishing the correct value for the anomalous dimension of the quark mass obtained (for an earlier treatment along the same lines, see [3]). The main upshot of these arguments for our present purposes is that, just as  $\mathcal{Q}(q, -p_1, p_3)$  and  $\widehat{d}(q^2)$ , the quantity  $K_{\text{gap}}(-k, k+p, -p)$  defined in Eq. (7.9) is also  $\mu$ -independent. In fact,  $K_{\text{gap}}(-k, k+p, -p)$  is composed of two individually  $\mu$ -independent factors, namely

$$K_{\text{gap}} = \left\{ \alpha_s^{1/2}(\mu) \Delta^{1/2}(k^2) \left[ \frac{L_1(-k, k+p, -p)}{A(p+k)} \right] \right\} \left[ \alpha_s^{1/2}(\mu) \Delta^{1/2}(k^2) F(k^2) \right]. \quad (7.10)$$

Evidently, the combination in curly brackets is essentially  $\mathcal{Q}^{1/2}$ , while the one in square brackets is RGI due to the nonperturbative relation that holds between  $F$  and  $1+G$ , as discussed in detail in [66].

A representative case of  $K_{\text{gap}}(p_1, p_2, \theta)$  when  $\theta = \pi/6$  is shown on the left panel of Fig. 24, while on the right panel we show the dimensionless quantity  $q^2 K_{\text{gap}}(p_1, p_2, \pi/6)$ , which is the 3-D analogue of  $\mathcal{I}_{\mathcal{Q}}(q^2)$  and  $\mathcal{I}_{\widehat{d}}(q^2)$ .

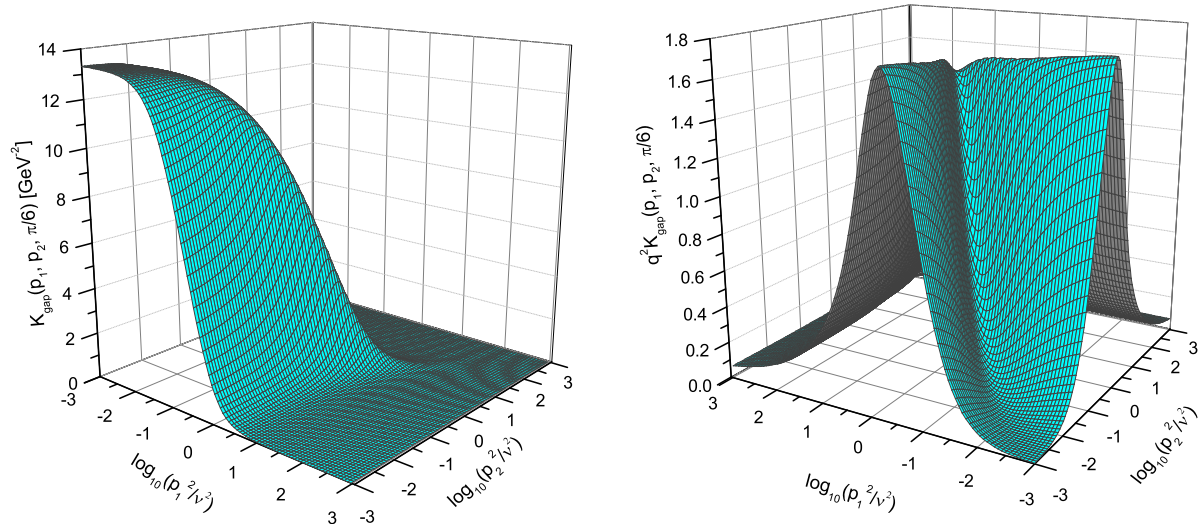


FIG. 24. The kernel  $K_{\text{gap}}(p_1, p_2, \pi/6)$  defined in Eq. (7.9) (left panel), and its dimensionless counterpart  $q^2 K_{\text{gap}}(p_1, p_2, \pi/6)$  (right panel).

We clearly see that  $q^2 K_{\text{gap}}(p_1, p_2, \pi/6)$  displays two symmetric peaks, which appear when one of the momenta (either  $p_1$  or  $p_2$ ) vanishes and the other is of the order of 730 MeV. For

other values of  $\theta$  we found a similar pattern. Therefore, it is reasonable to expect that the gap equation will receive more support around this region.

We end this section by emphasizing that a complete treatment of both BSE and gap equations requires the inclusion of all vertex form factors (the four non-transverse and the eight transverse ones). Moreover, both equations involve an angular integration over  $\theta$ ; consequently, variations in the angular structure of the twelve form factors may have a significant impact on the phenomenological parameters produced. Therefore, the analysis presented in the section should serve as a simple rough estimate of the possible impact of a unique form-factor, namely  $L_1$ .

## VIII. DISCUSSION AND CONCLUSIONS

We have presented a novel nonperturbative computation of the “non-transverse” components of the quark-gluon vertex, for general values of the Euclidean momenta entering in them. The starting point of this analysis is the STI that the quark-gluon vertex satisfies, which determines completely its four form factors in terms of the quark propagator, the ghost dressing function, and the quark-ghost scattering kernel. The inclusion of these last two ghost-related quantities implements the non-Abelian conversion of the usual QED-inspired BC Ansatz employed for the quark-gluon vertex. Even though the procedure we have followed is in principle applicable for any value of the gauge fixing parameter, in practice all ingredients relevant to the calculation have been computed in the Landau gauge. The form factors of the quark-ghost scattering kernel have been computed within the “one-loop dressed” approximation, which involves a single diagram, where all propagators are fully dressed, while certain simplifying approximations have been employed for the corresponding vertices. The results obtained, displayed in various 3-D plots, indicate considerable deviations from the Abelian BC expressions. In addition, several typical kinematic configurations considered in the related literature, such as the “soft gluon” or “symmetric” limits, have been extracted from the general 3-D results through appropriate 2-D “projections”.

The most natural context where the results of the present analysis may be applied is the study of chiral symmetry breaking and dynamical quark mass generation by means of the standard Landau gauge gap equation, along the lines presented in subsection VII C, where, however, only the effect of a special kinematic configuration of  $L_1$  was considered. Of course,

the precise 3-D form of all form factors is bound to affect the overall strength of the kernel of the gap equation, and the ensuing integration over virtual momenta will “peak” the strength of the full kernel around a particular mass-scale, whose value, as is well-known, is crucial for the final amount of quark mass that can be generated dynamically. Note, in particular, that in an earlier approach [4] a rudimentary version of the non-Abelian BC vertex was constructed by setting  $X_1 = X_2 = X_3 = 0$ , and using only a particular 2-D “slice” of  $X_0$ . The gap equation with this particular vertex gave rise to a running quark mass,  $\mathcal{M}(q^2)$ , whose value at the origin was  $\mathcal{M}(0) \approx 300$  MeV, when the value of the strong coupling used was  $\alpha_s \approx 0.29$ . It would be therefore important to study the same issue using instead the more complete version of the non-Abelian BC vertex obtained in the present work. In fact, a detailed analysis of the gap equation combining the non-Abelian BC part derived here and the purely transverse part employed in [59], imposing the physical constraints applied in this latter work, may single out a rather limited set of the possible vertex Ansätze that would be compatible with contemporary QCD phenomenology.

An additional issue, related to the present work as well as the prospect of applying the results to the study of the gap equation, has to do with the treatment of the set of dynamical equations that enter into the problem under study. In particular, one of the main technical shortcomings of the present work is the treatment of the Dirac components of the quark propagator [ $A(p^2)$  and  $\mathcal{M}(q^2)$ ], shown in Fig. (5) as *external quantities*, in the sense that they were obtained from a gap equation that was solved in isolation, using an Ansatz for the quark-gluon vertex corresponding precisely to the simplified non-Abelian BC vertex mentioned above [4]. The amelioration of this drawback requires the treatment of all dynamical equations involved as a system of coupled integral equations, whose simultaneous solution must be determined through numerical iteration. We hope to be able to report considerable progress in this direction in the near future.

## ACKNOWLEDGMENTS

The research of J. P. is supported by the Spanish Ministerio de Economía y Competitividad (MEYC) under grants FPA2014-53631-C2-1-P and SEV-2014-0398, and Generalitat Valenciana under grant Prometeo II/2014/066. The work of A. C. A, J. C. C. and M. N. F. are supported by the Brazilian National Council for Scientific and Technological Development

(CNPq) under the grants 305815/2015, 141981/2013-0 and 147433/2014-2, respectively. The authors thank D. Binosi for valuable communications. This research was performed using the Feynman Cluster of the John David Rogers Computation Center (CCJDR) in Institute of Physics “Gleb Wataghin”, University of Campinas.

### Appendix A: Taylor expansions of $\mathcal{K}$

In this Appendix we outline the Taylor expansions of Eq. (3.21) needed for the derivation of certain special kinematic limits. For concreteness we will work in some detail the derivation of the  $X_i$  in the soft gluon and the quark symmetric cases, which, as discussed in the section V, are obtained by taking the limit  $\sin \theta \rightarrow 0$  in Eq. (3.21). The corresponding expansions of  $\mathcal{K}$  around  $p_1 = 0$  ( $p_2 = 0$ ), relevant for the soft anti-quark (quark) configuration, proceed following completely analogous steps.

Consider the Eq. (3.21), and expand the kernel  $\mathcal{K}(p_1, p_2, l)$  around  $\sin \theta = 0$ ,

$$\mathcal{K}(p_1, p_2, l) = \mathcal{K}_0 + \sin \theta \mathcal{K}'_0 + \mathcal{O}(\sin^2 \theta), \quad (\text{A1})$$

where we have introduced the compact notation

$$\mathcal{K}_0 = \mathcal{K}(p_1, p_2, l) \Big|_{\sin \theta=0}, \quad \mathcal{K}'_0 = \frac{\partial \mathcal{K}(p_1, p_2, l)}{\partial \sin \theta} \Big|_{\sin \theta=0},$$

Concentrating on the contribution of  $\mathcal{K}_0$  in Eqs. (3.11), we clearly see that the only dependence of  $\mathcal{K}(p_1, p_2, l)$  on  $\varphi_2$  stems from  $D(l - p_1)$ , namely

$$D(l - p_1) = D(l^2 + p_1^2 - 2lp_1[\cos \theta \cos \varphi_1 + \sin \theta \sin \varphi_1 \cos \varphi_2]). \quad (\text{A2})$$

Thus, in the limit  $\sin \theta = 0$ ,  $\mathcal{K}_0$  is completely independent of  $\varphi_2$ , and the integration over this variable becomes trivial. Then we notice that, in the expressions for  $X_i$ , the terms with a  $\sin \theta$  in the denominator are always proportional to  $\cos \varphi_2$ , which leads to the following vanishing angular integration

$$\int_0^\pi d\varphi_2 \sin \varphi_2 \cos \varphi_2 = 0. \quad (\text{A3})$$

Therefore, all contributions of the Eq. (3.11) containing  $\mathcal{K}_0$  are finite. Evidently, the contribution of the second term in the expansion of Eq. (A1) is automatically finite, given that it is explicitly multiplied by a  $\sin \theta$  that cancels directly the corresponding term in the denominator of  $\mathcal{K}$ .

Implementing the above procedure in Eq. (3.21), we find that the form factors in the limit  $\sin \theta = 0$  reduce to

$$\begin{aligned}
X_0(p_1, p_2, \theta = 0, \pi) &= 1 + \frac{C_A g^2}{4} \int_{l_E} \frac{A(l^2)}{s^2} \mathcal{K}_0 \{ p_2^2 l^2 \sin^2 \varphi_1 - (l - p_2)^2 p_1 p_2 \cos \theta \\
&\quad + [p_1 l \cos \theta \cos \varphi_1 - p_1 p_2 \cos \theta] (p_2 l \cos \varphi_1 - p_2^2) \} , \\
X_1(p_1, p_2, \theta = 0, \pi) &= \frac{C_A g^2}{4} \int_{l_E} \frac{B(l^2)}{s^2} \left\{ \mathcal{K}_0 [s^2 - l^2 \sin^2 \varphi_1 \cos^2 \varphi_2] \right. \\
&\quad \left. + l(l \cos \varphi_1 - p_2) \left( \frac{p_2}{p_1} - \cos \theta \right) \mathcal{K}'_0 \sin \varphi_1 \cos \varphi_2 \right\} , \\
X_2(p_1, p_2, \theta = 0, \pi) &= \frac{C_A g^2}{4} \int_{l_E} \frac{B(l^2)}{s^2} \left\{ \mathcal{K}_0 \left[ (l \cos \varphi_1 - p_2)^2 \left( 1 - \frac{p_1}{p_2} \cos \theta \right) - s^2 \right. \right. \\
&\quad \left. \left. + \frac{p_1 l^2}{p_2} \cos \theta \sin^2 \varphi_1 \cos^2 \varphi_2 \right] - l(l \cos \varphi_1 - p_2) \cos \theta \left( 1 - \frac{p_1}{p_2} \cos \theta \right) \mathcal{K}'_0 \sin \varphi_1 \cos \varphi_2 \right\} , \\
X_3(p_1, p_2, \theta = 0, \pi) &= \frac{C_A g^2}{4} \int_{l_E} \frac{A(l^2)}{s^2} \left\{ \mathcal{K}_0 \left[ l^2 \sin^2 \varphi_1 \cos^2 \varphi_2 - s^2 \frac{l}{p_2} \cos \varphi_1 \right] \right. \\
&\quad \left. - l^2 (l - p_2 \cos \varphi_1) \left( \frac{1}{p_1} - \frac{\cos \theta}{p_2} \right) \mathcal{K}'_0 \sin \varphi_1 \cos \varphi_2 \right\} . \tag{A4}
\end{aligned}$$

where the variable  $s^2$  was defined below Eq. (3.21). For the actual determination of  $\mathcal{K}'_0$ , note that

$$\left. \frac{\partial D(l - p_1)}{\partial \sin \theta} \right|_{\sin \theta = 0} = -2l p_1 \sin \varphi_1 \cos \varphi_2 \frac{\partial D(l)}{\partial l^2} , \tag{A5}$$

so that

$$\mathcal{K}'_0 = -2l p_1 \sin \varphi_1 \cos \varphi_2 \frac{[A(l^2) + A(p_2^2)]}{A^2(l^2)l^2 + B^2(l^2)} \Delta(l - p_2) \frac{\partial D(l)}{\partial l^2} . \tag{A6}$$

Note finally that, since in both the soft gluon and the quark-symmetric limits we have  $p_1 = p_2$ , the difference between the two depends on the value that  $\theta$  will acquire in Eq. (A4), namely  $\theta = 0$  or  $\theta = \pi$ , respectively.

- 
- [1] P. Maris and C. D. Roberts, *Int. J. Mod. Phys. E* **12**, 297 (2003).
  - [2] C. D. Roberts and A. G. Williams, *Prog. Part. Nucl. Phys.* **33**, 477 (1994).
  - [3] C. S. Fischer and R. Alkofer, *Phys. Rev. D* **67**, 094020 (2003).
  - [4] A. C. Aguilar and J. Papavassiliou, *Phys. Rev. D* **83**, 014013 (2011).

- [5] I. C. Cloet and C. D. Roberts, *Prog. Part. Nucl. Phys.* **77**, 1 (2014).
- [6] P. Maris and P. C. Tandy, *Phys. Rev. C* **60**, 055214 (1999).
- [7] A. Bender, W. Detmold, C. D. Roberts and A. W. Thomas, *Phys. Rev. C* **65**, 065203 (2002).
- [8] R. Williams, C. S. Fischer and W. Heupel, *Phys. Rev. D* **93**, no. 3, 034026 (2016).
- [9] G. Eichmann, H. Sanchis-Alepuz, R. Williams, R. Alkofer and C. S. Fischer, *Prog. Part. Nucl. Phys.* **91**, 1 (2016).
- [10] H. Sanchis-Alepuz and R. Williams, *Phys. Lett. B* **749**, 592 (2015).
- [11] M. S. Bhagwat, A. Holl, A. Krassnigg, C. D. Roberts and P. C. Tandy, *Phys. Rev. C* **70**, 035205 (2004).
- [12] A. Holl, A. Krassnigg and C. D. Roberts, *Nucl. Phys. Proc. Suppl.* **141**, 47 (2005).
- [13] L. Chang and C. D. Roberts, *Phys. Rev. Lett.* **103**, 081601 (2009).
- [14] R. Williams, *Eur. Phys. J. A* **51**, no. 5, 57 (2015).
- [15] A. Bender, C. D. Roberts and L. Von Smekal, *Phys. Lett. B* **380**, 7 (1996).
- [16] M. Hopfer, A. Windisch and R. Alkofer, *PoS ConfinementX* , 073 (2012).
- [17] M. S. Bhagwat and P. C. Tandy, *Phys. Rev. D* **70**, 094039 (2004).
- [18] F. J. Llanes-Estrada, C. S. Fischer and R. Alkofer, *Nucl. Phys. Proc. Suppl.* **152**, 43 (2006).
- [19] R. Alkofer, C. S. Fischer, F. J. Llanes-Estrada and K. Schwenzer, *Annals Phys.* **324**, 106 (2009).
- [20] H. H. Matevosyan, A. W. Thomas and P. C. Tandy, *Phys. Rev. C* **75**, 045201 (2007).
- [21] A. C. Aguilar, D. Binosi, J. C. Cardona and J. Papavassiliou, *PoS ConfinementX* , 103 (2012).
- [22] E. Rojas, J. P. B. C. de Melo, B. El-Bennich, O. Oliveira and T. Frederico, *JHEP* **1310**, 193 (2013).
- [23] C. S. Fischer, *J. Phys. G* **32**, R253 (2006).
- [24] A. Salam, *Phys. Rev.* **130**, 1287 (1963).
- [25] A. Salam and R. Delbourgo, *Phys. Rev.* **135**, B1398 (1964).
- [26] R. Delbourgo and P. C. West, *J. Phys. A* **10**, 1049 (1977).
- [27] R. Delbourgo and P. C. West, *Phys. Lett. B* **72**, 96 (1977).
- [28] D. C. Curtis and M. R. Pennington, *Phys. Rev. D* **42**, 4165 (1990).
- [29] A. Bashir, A. Kizilersu and M. R. Pennington, *Phys. Rev. D* **57**, 1242 (1998).
- [30] A. Kizilersu and M. R. Pennington, *Phys. Rev. D* **79**, 125020 (2009).
- [31] J. S. Ball and T. W. Chiu, *Phys. Rev. D* **22**, 2542 (1980).

- [32] A. C. Aguilar, D. Binosi, D. Ibañez and J. Papavassiliou, Phys. Rev. D **90**, no. 6, 065027 (2014).
- [33] W. Heupel, T. Goecke and C. S. Fischer, Eur. Phys. J. A **50**, 85 (2014).
- [34] J. Braun, L. Fister, J. M. Pawłowski and F. Rennecke, Phys. Rev. D **94**, no. 3, 034016 (2016).
- [35] M. Mitter, J. M. Pawłowski and N. Strodthoff, Phys. Rev. D **91**, 054035 (2015).
- [36] J. Skullerud, P. O. Bowman and A. Kizilersu, hep-lat/0212011.
- [37] J. Skullerud and A. Kizilersu, JHEP **0209**, 013 (2002).
- [38] J. I. Skullerud, P. O. Bowman, A. Kizilersu, D. B. Leinweber and A. G. Williams, JHEP **0304**, 047 (2003).
- [39] J. I. Skullerud, P. O. Bowman, A. Kizilersu, D. B. Leinweber and A. G. Williams, Nucl. Phys. Proc. Suppl. **141**, 244 (2005).
- [40] H. W. Lin, Phys. Rev. D **73**, 094511 (2006).
- [41] A. Kizilersu, D. B. Leinweber, J. I. Skullerud and A. G. Williams, Eur. Phys. J. C **50**, 871 (2007).
- [42] O. Oliveira, A. Kizilersu, P. J. Silva, J. I. Skullerud, A. Sternbeck and A. G. Williams, arXiv:1605.09632 [hep-lat].
- [43] A. Sternbeck, P. H. Balduf, A. Kizilersu, O. Oliveira, P. J. Silva, J. I. Skullerud and A. G. Williams, arXiv:1702.00612 [hep-lat].
- [44] A. I. Davydychev, P. Osland and L. Saks, Phys. Rev. D **63**, 014022 (2001).
- [45] J. A. Gracey, Phys. Rev. D **90**, no. 2, 025014 (2014).
- [46] R. Bermudez, L. Albino, L. X. Gutierrez-Guerrero, M. E. Tejeda-Yeomans and A. Bashir, Phys. Rev. D **95**, no. 3, 034041 (2017).
- [47] K. G. Chetyrkin and T. Seidensticker, Phys. Lett. B **495**, 74 (2000).
- [48] K. G. Chetyrkin and A. Retey, hep-ph/0007088.
- [49] I. L. Bogolubsky, E. M. Ilgenfritz, M. Muller-Preussker and A. Sternbeck, PoS **LAT2007**, 290 (2007).
- [50] A. Bashir, R. Bermudez, L. Chang and C. D. Roberts, Phys. Rev. C **85**, 045205 (2012).
- [51] L. Chang, C. D. Roberts and S. M. Schmidt, Phys. Rev. C **87**, no. 1, 015203 (2013).
- [52] L. Chang, Y. X. Liu and C. D. Roberts, Phys. Rev. Lett. **106**, 072001 (2011).
- [53] Y. Takahashi, “Canonical Quantization and Generalized Ward Relations: Foundation Of Non-perturbative Approach,” Positano Symp.1985:0019.

- [54] K. I. Kondo, *Int. J. Mod. Phys. A* **12**, 5651 (1997).
- [55] H. X. He, F. C. Khanna and Y. Takahashi, *Phys. Lett. B* **480**, 222 (2000).
- [56] M. R. Pennington and R. Williams, *J. Phys. G* **32**, 2219 (2006).
- [57] H. X. He, *Commun. Theor. Phys.* **46**, 109 (2006).
- [58] S. X. Qin, L. Chang, Y. X. Liu, C. D. Roberts and S. M. Schmidt, *Phys. Lett. B* **722**, 384 (2013).
- [59] D. Binosi, L. Chang, J. Papavassiliou, S. X. Qin and C. D. Roberts, arXiv:1609.02568 [nucl-th].
- [60] A. Kizilersu, M. Reenders and M. R. Pennington, *Phys. Rev. D* **52**, 1242 (1995).
- [61] A. C. Aguilar, D. Binosi and J. Papavassiliou, *Phys. Rev. D* **84**, 085026 (2011).
- [62] A. C. Aguilar, D. Ibañez and J. Papavassiliou, *Phys. Rev. D* **87**, no. 11, 114020 (2013).
- [63] A. C. Aguilar, D. Binosi and J. Papavassiliou, *Phys. Rev. D* **86**, 014032 (2012).
- [64] J. M. Cornwall, *Phys. Rev. D* **26**, 1453 (1982).
- [65] A. C. Aguilar, D. Binosi and J. Papavassiliou, *Phys. Rev. D* **78**, 025010 (2008).
- [66] A. C. Aguilar, D. Binosi, J. Papavassiliou and J. Rodriguez-Quintero, *Phys. Rev. D* **80**, 085018 (2009).
- [67] A. C. Aguilar, J. C. Cardona, M. N. Ferreira and J. Papavassiliou, arXiv:1610.06158 [hep-ph].
- [68] A. Sternbeck, E.-M. Ilgenfritz, M. Muller-Preussker and A. Schiller, *Phys. Rev. D* **72**, 014507 (2005).
- [69] O. Nachtmann and W. Wetzel, *Nucl. Phys. B* **187**, 333 (1981).
- [70] D. Binosi, L. Chang, J. Papavassiliou and C. D. Roberts, *Phys. Lett. B* **742**, 183 (2015).
- [71] P. A. Grassi, T. Hurth and M. Steinhauser, *Annals Phys.* **288**, 197 (2001).
- [72] D. Binosi and J. Papavassiliou, *Phys. Rev. D* **66**, 025024 (2002).
- [73] D. Binosi and J. Papavassiliou, *Phys. Rept.* **479**, 1 (2009).
- [74] A. C. Aguilar, D. Binosi and J. Papavassiliou, *JHEP* **1007**, 002 (2010).
- [75] S. x. Qin, L. Chang, Y. x. Liu, C. D. Roberts and D. J. Wilson, *Phys. Rev. C* **84**, 042202 (2011).
- [76] P. Boucaud, F. De Soto, J. P. Leroy, A. Le Yaouanc, J. Micheli, O. Pene and J. Rodriguez-Quintero, *Phys. Rev. D* **79**, 014508 (2009).